Cuprate diamagnetism in the presence of a pseudogap: Beyond the standard fluctuation formalism

Rufus Boyack,[1] Qijin Chen,[1,2] A. A. Varlamov,[3] and K. Levin[1]
[1]*James Franck Institute, University of Chicago, Chicago, Illinois 60637, USA*
[2]*Zhejiang Institute of Modern Physics and Department of Physics, Zhejiang University, Hangzhou, Zhejiang 310027, China*
[3]*CNR-SPIN (Istituto Superconduttori, Materiali Innovativi e Dispositivi), Viale del Politecnico 1, I-00133 Rome, Italy*

(Received 9 October 2017; published 1 February 2018)

It is often claimed that among the strongest evidence for preformed-pair physics in the cuprates are the experimentally observed large values for the diamagnetic susceptibility and Nernst coefficient. These findings are most apparent in the underdoped regime, where a pseudogap is also evident. While the conventional (Gaussian) fluctuation picture has been applied to address these results, this preformed-pair approach omits the crucial effects of a pseudogap. In this paper we remedy this omission by computing the diamagnetic susceptibility and Nernst coefficient in the presence of a normal state gap. We find a large diamagnetic response for a range of temperatures much higher than the transition temperature. In particular, we report semiquantitative agreement with the measured diamagnetic susceptibility onset temperatures, over the entire range of hole dopings. Notable is the fact that at the lower critical doping of the superconducting dome, where the transition temperature vanishes and the pseudogap onset temperature remains large, the onset temperature for both diamagnetic and transverse thermoelectric transport coefficients tends to zero. Due to the importance attributed to the cuprate diamagnetic susceptibility and Nernst coefficient, this work helps to clarify the extent to which pairing fluctuations are a component of the cuprate pseudogap.

DOI: 10.1103/PhysRevB.97.064503

I. INTRODUCTION AND OVERVIEW OF RESULTS

Establishing the origin of the cuprate pseudogap is a long-standing problem in the field of high-T_c superconductivity [1]. At its heart is the central issue of whether this pseudogap arises from precursor superconductivity or from an alternative order parameter. In support of this latter viewpoint is an increasing number of experiments showing evidence for (finite-range) charge-density-wave order [2,3]. With the application of a magnetic field this order appears to be stabilized [4], although there is evidence the pseudogap itself remains intact.

On the other hand, there is also mounting support for the first viewpoint: the origin of the cuprate pseudogap is a precursor-pairing scenario. The conventional fluctuation formalism [5], used to support preformed-pair physics in the cuprates, provides a natural explanation for the anomalously large diamagnetic susceptibility and large Nernst coefficient observed above T_c [6,7]. However, this standard fluctuation theory is a weak-fluctuation approach that largely ignores the substantial normal state gap, which is of fundamental interest here and observed in a variety of experiments. As a result it is not expected to be valid in the doping regimes where such a gap is present.

This leads to the challenge addressed in this paper of going beyond the weak-fluctuation formalism within a precursor-pairing approach. Here we compute the diamagnetic susceptibility and transverse thermoelectric coefficient by applying a BCS-BEC crossover [8–10] scheme above T_c. This crossover scenario, built on a natural generalization [11] of the BCS ground state, incorporates the variation from weak to strong attractive interactions between the underlying fermionic constituents. In this context, Leggett [12] states in his summary article about the copper oxide superconductors, "The small size of the cuprate pairs puts us in the intermediate regime of the so-called BEC-BCS crossover." It is important to emphasize at the outset that the pseudogap phase for the d-wave cuprates is also well outside the BEC regime [8,13]. Rather, the pseudogap phase represents an intermediate state between the BCS and BEC regimes.

There is a substantial body of literature on the diamagnetic susceptibility and Nernst coefficient in the cuprates. The early seminal experiments [6,14] first associated the Nernst response with vortex excitations. The diamagnetic susceptibility [7] was similarly interpreted as reflecting some form of normal state Cooper pairing. More recent experimental emphasis has been on the interplay of vortex excitations with charge-density-wave order [15,16]. While other alternatives have been contemplated [17], a large number of theories addressing these experiments have been based on a preformed-pair formalism. This preformed-pair approach is associated with superconducting fluctuation contributions [5] to the diamagnetic [18] and Nernst [19] responses.

However, in the context of transport the preformed-pair scenario has dealt almost exclusively with a weak-fluctuation formalism [5], considering only the lowest order fluctuation contributions to the electromagnetic (EM) response. In the absence of impurities, these consist of two density of states (DOS), one Maki-Thompson (MT) and two identical Aslamazov-Larkin (AL) diagrams. For the diamagnetic susceptibility and the Nernst coefficient, it is found that the singular contribution arises from the Aslamazov-Larkin diagrams [5,20,21]. These results can be equivalently derived from Gaussian-fluctuation theory, which is associated with time-dependent Ginzburg-Landau theory [22].

There is also related work based on phase-only fluctuations [23] within a two-dimensional BKT-like theory; phase fluctuations are thought to dominate their amplitude counterparts in the vicinity of T_c [24], and one presumes here that mobile vortices are the fundamental constituents. Another preformed pair approach [25], based on the so-called "Hartree" approximation to Ginzburg-Landau theory, has been used with some success to address diamagnetism in the cuprates. It should be noted there is an established relation [26] between this phenomenological Hartree scheme and the present microscopic approach in the limit that the pairing gap at the transition is small.

Stronger pairing effects in transport have been included in differing contexts [28–30], all of which build on a fluctuation scenario. The authors of Ref. [28] introduced pseudogap self-energy effects in the standard Aslamazov-Larkin diagrams by correcting the so-called EM "triangle" vertex, which represents an effective bosonic EM vertex. In Secs. V and VI of the paper this approach is discussed in more detail, where it is noted that correcting this vertex without simultaneously correcting the pair propagator is inconsistent. An alternative diagrammatic approach was studied in Ref. [29], which investigated the diamagnetic susceptibility associated with the fermionic quasiparticles in the presence of a pseudogap. This approach misses the essential physics of the bosonic fluctuations which, as Sec. V shows, are found to be the singular contribution.

Finally, the authors of Ref. [30] introduced an extension of the Gaussian-fluctuation formalism [22] by computing the transport properties of independent, noncondensed bosons in contact with a Leggett-Caldeira particle bath. This bath leads to an interconversion with the bosons so that the boson number is no longer fixed. The bath approach is a phenomenological treatment of transport in which the reservoir yields finite-lifetime effects, and simulates the role of paired fermions or composite bosons.

In contrast, in this paper we present a microscopic theory of electromagnetic and thermoelectric transport, based on a fluctuation formalism which more naturally includes the contribution of a pseudogap associated with fermion pairs. While the standard weak-fluctuation formalism relates in some ways to the physics of the present paper, we emphasize that widespread pseudogap effects are absent in the associated correlation functions; this is because they involve only non-interacting fermionic Green's functions.

These observations are illustrated in the top row of Fig. 1, which provides a more graphic physical picture of the fluctuation-BCS, the pseudogap, and the BEC regimes. Below we refer to the fluctuation-BCS limit as the "BCS limit." Strictly speaking, it goes beyond mean-field BCS theory and serves as the basis for the conventional fluctuation picture. In the intermediate, or pseudogap, regime, the system is fermionic with a positive chemical potential $\mu \gg (\Delta_0, T_c)$, where Δ_0 is the fermionic excitation gap at $T = 0$. An important fact, however, is that at the onset of condensation there is a nonzero gap (pseudogap) in the fermionic excitation spectrum. The distinction between BCS and BEC leads to different behavior of the pair propagator (or t matrix) [27], $t(q)$, associated with composite bosons. Plotted in row (a) of Fig. 1 is $-\mathrm{Im}\, t(\Omega, \mathbf{q} = 0)$ slightly above T_c, illustrating the differences in the composite boson propagator in these regimes.

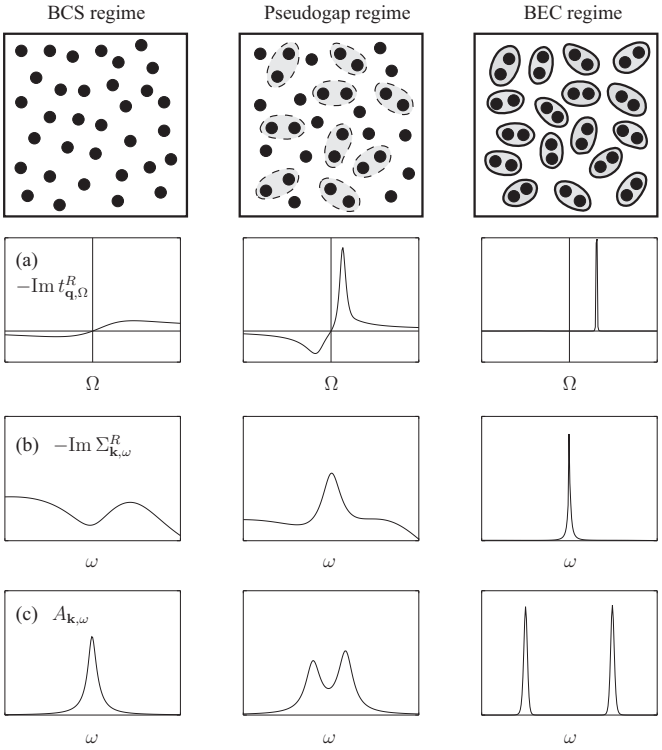

FIG. 1. Evolution from the weak-coupling BCS through the pseudogap to the strong-coupling BEC regimes for the excitations. The figure shows the corresponding [row (a)] pair excitation spectrum $-\mathrm{Im}\, t(\Omega, \mathbf{q} = 0)$, [row (b)] imaginary part of the fermionic self-energy $-\mathrm{Im}\, \Sigma(\omega, \mathbf{k})$, and [row (c)] fermionic spectral function $A(\omega, \mathbf{k})$ at the Fermi level for T slightly above T_c. This figure is taken from Ref. [27].

At small four-vector $q^\mu = (\Omega, \mathbf{q})$, the inverse (retarded) pair propagator can be generically written as

$$t^{-1}(q) \approx Z[\kappa\Omega - \mathbf{q}^2/(2M_{\mathrm{pair}}) - |\mu_{\mathrm{pair}}| + i\Gamma\Omega]. \quad (1.1)$$

Here the coefficients κ and Γ are real and dimensionless. The real part defines an effective pair mass, M_{pair}, and a pair chemical potential, $\mu_{\mathrm{pair}} \propto t^{-1}(0)$, whereas the imaginary part, $\propto \Gamma\Omega$, represents the diffusive contribution to the inverse pair propagator [31]. Our final results show that the overall coefficient of proportionality, Z, is irrelevant; only the ratio between $1/M_{\mathrm{pair}}$ and μ_{pair} (as well as the ratio κ/Γ) appear. In the BCS (BEC) limit the parameter Γ, which reflects the damping of the pairs, is very large (small) compared to κ. Here we presume this damping derives from interactions with the fermions. In the conventional fluctuation literature [5] the fluctuating Cooper pairs are diffusive with a purely imaginary dispersion, so that $\kappa = 0$ and $\Gamma \propto \pi/(8T_c)$. In general, $\kappa \neq 0$ reflects particle-hole asymmetry.

From a microscopic point of view the pair propagator of the weak-fluctuation theory depends on two bare Green's functions. However, in the presence of a pseudogap one or more dressed Green's functions, which contain the pairing self-energy associated with the pseudogap, enters into the pair propagator. This leads to a different pair lifetime, mass, and chemical potential compared to the weak-fluctuation case.

These distinctions then appear in response functions and in the associated transport coefficients.

It is useful in this overview section to present the central results of this paper for the diamagnetic susceptibility, $\chi_{\rm dia}$:

$$\chi_{\rm dia} = -\frac{k_B T (2e)^2}{24\pi\hbar c^2}\sqrt{\frac{1/(2M_{\rm pair})}{|\mu_{\rm pair}|}}, \tag{1.2}$$

and similarly the transverse thermoelectric coefficient (related to the Nernst coefficient), $\widetilde{\alpha}_{xy}$:

$$\widetilde{\alpha}_{xy} = \frac{B k_B T e^2}{12\pi\hbar^2 c}\sqrt{\frac{1/(2M_{\rm pair})}{|\mu_{\rm pair}|}}\left(\frac{3\kappa^2+\Gamma^2}{\Gamma^2}\right). \tag{1.3}$$

These expressions, obtained for three-dimensional (3D) clean systems, are valid in the small $|\mu_{\rm pair}|$ limit: ($|\mu_{\rm pair}| \ll T_c$). The size of the diamagnetic susceptibility and transverse thermoelectric coefficient are determined by two key parameters: the pair mass $M_{\rm pair}$ (related to the inverse coherence length, often appearing as an inverse diffusion coefficient in the weak-fluctuation literature) and the pair chemical potential $\mu_{\rm pair}$.

The rest of this paper is organized as follows. In Sec. II the pair propagator and associated properties of the normal state are characterized as the pairing varies from weak to strong attraction. Sections III and IV show how our pseudogap formalism is implemented in the diamagnetic response, while in Sec. V the diamagnetic susceptibility is calculated in the small-$|\mu_{\rm pair}|$ limit. The analogous calculations for the transverse thermoelectric coefficient are discussed in Sec. VI. Our numerical results for the phase diagram and diamagnetic susceptibility onset temperature are then presented in Sec. VII along with a comparison with experiment. Finally in Sec. VIII our conclusions are outlined.

II. PAIR-PROPAGATOR FORMALISM

In this section we give a brief overview of the pair-fluctuation formalism underlying the work in this paper. For a more extensive and thorough review, see Refs. [9,10]. At the heart of any calculation incorporating bosonic degrees of freedom into diamagnetic susceptibility and general electromagnetic transport is the explicit form of the pair propagator. We emphasize that the BCS mean-field gap equation provides important intuition about the form this fluctuation propagator should take. In the standard BCS mean-field theory the pairing gap parameter is exactly equal to the order parameter. More generally, a nonzero pairing gap will be present at the onset of condensation. Importantly, this pairing gap Δ must be continuous across T_c in order to properly describe a second-order phase transition. This normal state, in which the pairing gap persists, represents the pseudogap phase.

We begin with a generic system of electrons characterized by an effective, short-range pairing interaction with a grand canonical Hamiltonian

$$H - \mu N = \sum_{\mathbf{k}\sigma}\xi_{\mathbf{k}} c^\dagger_{\mathbf{k}\sigma} c_{\mathbf{k}\sigma} + \sum_{\mathbf{k}\mathbf{k}'\mathbf{q}} V_{\mathbf{k},\mathbf{k}'} c^\dagger_{\mathbf{k}+\mathbf{q}/2\uparrow} c^\dagger_{-\mathbf{k}+\mathbf{q}/2\downarrow} c_{-\mathbf{k}'+\mathbf{q}/2\downarrow} c_{\mathbf{k}'+\mathbf{q}/2\uparrow}, \tag{2.1}$$

where $c^\dagger_{\mathbf{k}\sigma}$ ($c_{\mathbf{k}\sigma}$) creates (annihilates) an electron in the momentum state $\mathbf{k}$ with spin σ, and $\xi_{\mathbf{k}}$ is the energy dispersion measured with respect to the fermion chemical potential μ. For the cuprates, $\xi_{\mathbf{k}} = 2t(2-\cos k_x - \cos k_y) + 2t_z(1-\cos k_z) - \mu$, where t and t_z are the in-plane and out-of-plane hopping matrix elements, respectively, with $t_z \ll t$. The d-wave pairing interaction is given by $V_{\mathbf{k},\mathbf{k}'} = g\varphi_{\mathbf{k}}\varphi'_{\mathbf{k}}$ with $g<0$ and $\varphi_{\mathbf{k}} = \cos k_x - \cos k_y$ with lattice constant $a=1$. In the continuum case, $\xi_{\mathbf{k}} = \mathbf{k}^2/(2m) - \mu$ with m as the fermion mass. We set $\hbar = c = k_B = 1$ and restore these units at the end of the calculation. In what follows below, it is convenient to introduce the four-vector $k^\mu = (i\omega_n, \mathbf{k})$, where ω_n is a fermionic Matsubara frequency. Similarly, we define a generalized four-vector summation $\sum_k = T\sum_{i\omega_n}\sum_{\mathbf{k}}$.

The bare (inverse) single-particle Green's function, $G_0^{-1}(k)$, is given by $G_0^{-1}(k) = i\omega_n - \xi_{\mathbf{k}}$. The full Green's function, $G(k)$, is determined from the bare Green's function and self-energy, $\Sigma(k)$, through Dyson's equation: $G^{-1}(k) = G_0^{-1}(k) - \Sigma(k)$. In BCS mean-field theory, the self-energy has the form

$$\Sigma(k) = -\Delta^2 G_0(-k)\varphi^2_{\mathbf{k}} = \Delta^2\varphi^2_{\mathbf{k}}/(i\omega_n + \xi_{\mathbf{k}}). \tag{2.2}$$

Important here is the value of the pairing gap Δ which is constrained by the BCS mean-field gap equation. In the condensed phase [9] this can be written in a suggestive way as

$$g^{-1} + \sum_k G(k)G_0(-k)\varphi^2_{\mathbf{k}} = 0, \quad T \leqslant T_c. \tag{2.3}$$

Thus the gap equation in Eq. (2.3) can be viewed as a generalized Thouless criterion [32] for a pairing instability of the type $t^{-1}(q\to 0) = 0$. This implies that the (inverse) t matrix appropriate to BCS theory is

$$t^{-1}(q) \equiv g^{-1} + \sum_k G(k)G_0(-k+q)\varphi^2_{\mathbf{k}-\mathbf{q}/2}. \tag{2.4}$$

Here $q \equiv q^\mu = (i\Omega_m, \mathbf{q})$ (before analytic continuation), where Ω_m is a bosonic Matsubara frequency.

It follows directly from the gap equation in Eq. (2.3) that the t matrix associated with BCS theory involves one bare and one dressed Green's function. This asymmetric form, while perhaps surprising, has been derived in the literature [33] from a microscopic approach. The method implemented by Kadanoff and Martin was to study the equations of motion of the correlation functions, and use these to set up integral constraints on the many-particle Green's functions. The equation of motion for the single-particle Green's function depends on the two-particle Green's function, which in turn depends on the three-particle Green's function and so forth.

In order to truncate this infinite series of equations, Kadanoff and Martin considered a particular pairing scheme that approximates the three-particle correlation function solely in terms of the single-particle and two-particle Green's functions. In this approximation the relevant contributions are pairing interactions between fermions of opposite spins and momenta. From the integral equation for the two-particle Green's function, one can then derive the form of the t matrix given above. It is important to emphasize that the asymmetric combination of G_0 and G in the t matrix is essential to reproduce BCS theory. This shows that the presence of one dressed and one bare Green's function follows naturally from

this methodology. It is not an arbitrary choice. A review of the Kadanoff and Martin method can be found in Appendix A. Further details can also be found in Refs. [27,34].

We emphasize that this t matrix should be interpreted as the propagator for noncondensed fermion pairs associated with $q \neq 0$. At and below the condensation temperature the low-momentum noncondensed pairs become gapless [35] and thus acquire zero chemical potential. Since $t^{-1}(q=0) \propto \mu_{\rm pair}$, it follows that

$$t(q=0) = \infty, \quad T \leqslant T_c. \tag{2.5}$$

Thus the gap equation [Eq. (2.3)] can be equivalently written as a BEC condition:

$$\mu_{\rm pair} = 0, \quad T \leqslant T_c, \tag{2.6}$$

provided the self-energy appearing in $G(k)$ is given by the usual BCS form [Eq. (2.2)]. All of this general formalism is consistent with the generic form for the pair propagator in Eq. (1.1).

Now we connect the physics below T_c to that above T_c. In most t-matrix theories the associated fermionic self-energy is

$$\Sigma(k) = \sum_q t(q) G_0(-k+q) \varphi^2_{\mathbf{k}-\mathbf{q}/2}. \tag{2.7}$$

The quantity $t(q)$ is strongly peaked about $q=0$ as the transition is approached from above because $|\mu_{\rm pair}|$ is small; this allows the normal state self-energy to be written as $\Sigma(k) \approx -\Delta^2 G_0(-k)\varphi^2_{\mathbf{k}}$, with

$$\Delta^2 = -\sum_q t(q), \quad T \geqslant T_c. \tag{2.8}$$

With this result, the transition temperature T_c can then be computed. This is determined as the temperature at which the normal state value of Δ, given in Eq. (2.8), intersects with its value obtained at or below T_c, found from Eq. (2.3).

This physical picture is more complicated than in BCS mean-field theory because of the presence of a nonzero pseudogap at T_c, which must be continuous at a second-order phase transition. The parameters appearing in Eq. (1.1), such as the pair mass $M_{\rm pair}$, pair chemical potential $\mu_{\rm pair}$, and pair damping $\propto \Gamma$, can then be deduced from Eq. (2.4). It is crucial to include a self-consistently determined fermionic chemical potential using the number equation $n = 2\sum_k G(k)$. One can also define the pairing onset temperature T^* most naturally as the temperature at which Δ vanishes, as determined, for example, from the mean-field gap equation. In this way a phase diagram for T_c and T^*, as a function of band structure and interaction strength g, can be computed. This simultaneously yields the diamagnetic susceptibility and transverse thermoelectric coefficient via Eqs. (1.2) and (1.3). These limiting forms are derived in Secs. V and VI, while in Sec. VII of the paper the complete diamagnetic susceptibility expression is numerically calculated.

Finally, it is useful to contrast these pseudogap effects with the pair propagator for the more conventional weak-fluctuation theory. Aslamazov and Larkin [20] have written down the counterpart to Eq. (2.4) for the weak-fluctuation case, which in the d-wave limit is given by

$$t_0^{-1}(q) \equiv g^{-1} + \sum_k G_0(k) G_0(-k+q) \varphi^2_{\mathbf{k}-\mathbf{q}/2}. \tag{2.9}$$

In the pair propagator all fermionic Green's functions are bare and no pseudogap is present. In contrast to the strong-pairing limit, the above t matrix is associated with diffusive rather than propagating dynamics. Referring to Eq. (1.1), the parameter $\kappa = 0$, $|\mu_{\rm pair}| \propto (T - T_c)$, $\Gamma \propto \pi/(8T_c)$, and $1/(2M_{\rm pair}) \propto D$ (the diffusion constant).

In the $\kappa \to 0$ limit, instead of weakly damped and propagating noncondensed pairs, one has diffusive pair dynamics. This weak-attraction case, and its consequences for the fermionic properties [via Eq. (2.7)], is presented in the first column in Fig. 1. One can contrast the difference in behavior with that for the pseudogap case shown in the second column. Here the pairing strength has been increased relative to the first column and the associated t matrix acquires a significant propagating term (second row) with broken particle-hole symmetry.

The third row of the second column shows that the fermionic self-energy, deduced from Eq. (2.7), is reasonably well described by Eq. (2.2). Furthermore, the fermionic spectral function in the last row now has a double-peaked form associated with the presence of a normal state gap. The third column in Fig. 1 is appropriate to the strong-attraction case, $\Gamma \ll \kappa$, where the system is in the BEC regime. We reiterate that this is well outside [8] the physical parameter range associated with the d-wave paired cuprates.

To maintain clarity in the equations, in the following sections we present our theoretical derivations for short-range s-wave pairing in the 3D continuum with $\varphi_{\mathbf{k}} = 1$. However, our numerical results are for the quasi-2D d-wave case.

III. ELECTROMAGNETIC RESPONSE

We begin with a discussion of diamagnetic susceptibility, which represents the orbital current response to an external magnetic field. Here we use linear response theory to derive its Kubo formula. In the presence of a weak and externally applied EM vector potential, $A^\mu(q)$, the EM current is $j^\mu(q) = K^{\mu\nu}(q) A_\nu(q)$. The response kernel is $K^{\mu\nu}(q) = P^{\mu\nu}(q) + (n/m)\delta^{\mu\nu}(1-\delta_{\mu,0})$, with μ and ν not summed over. Here n is the particle number, determined from $n = 2\sum_k G(k)$, and $P^{\mu\nu}(q)$ are the EM response functions given by [36]

$$P^{\mu\nu}(q) = 2e^2 \sum_k G(k_+) \Gamma^\mu_{\rm E}(k_+,k_-) G(k_-) \gamma^\nu_{\rm E}(k_-,k_+). \tag{3.1}$$

Here e is the fermion charge. The bare EM vertex is $\gamma^\mu_{\rm E}(k_+,k_-)$ and the full EM vertex is $\Gamma^\mu_{\rm E}(k_+,k_-)$ [37], where $k_\pm = k \pm q/2$. The prefactor of 2 arises due to spin degeneracy for a spin-$\frac{1}{2}$ system of fermions.

An important relation between the full Green's function and the full EM vertex is the Ward-Takahashi identity (WTI) [38]:

$$\begin{aligned} q_\mu \Gamma^\mu_{\rm E}(k_+,k_-) &= G^{-1}(k_+) - G^{-1}(k_-) \\ &= q_\mu \gamma^\mu_{\rm E}(k_+,k_-) + \Sigma(k_-) - \Sigma(k_+). \end{aligned} \tag{3.2}$$

The bare WTI, $q_\mu \gamma^\mu_{\rm E}(k_+,k_-) = G_0^{-1}(k_+) - G_0^{-1}(k_-)$, is satisfied by the bare EM vertex $\gamma^\mu_{\rm E}(k_+,k_-) = (1,\mathbf{k}/m)$. For a neutral (charged) system with a global U(1) symmetry, the

corresponding conservation law is particle number (charge) conservation. The analysis here is for neutral superfluids. Satisfying the WTI is thus an important constraint which enforces conservation of global particle number. Applying the WTI to the response kernel $K^{\mu\nu}(q)$ yields $q_\mu K^{\mu\nu}(q)=0$; this is the statement of "gauge invariance."

In the $q\to 0$ limit, the WTI implies that $\Gamma^\mu_{\rm E}(k,k)=\gamma^\mu_{\rm E}(k,k)-\partial\Sigma(k)/\partial k_\mu$. Diagrammatically this relation asserts that the full EM vertex is determined by performing all bare EM vertex insertions in the self-energy diagram. In terms of components this expression becomes $\Gamma^0_{\rm E}(k,k)=\partial G^{-1}(k)/\partial\omega$ and $\Gamma^i_{\rm E}(k,k)=-\partial G^{-1}(k)/\partial k^i$.

It is straightforward to derive the diamagnetic susceptibility from these response functions. In the presence of a static external vector potential the magnetic field is $\mathbf{B}=i\mathbf{q}\times\mathbf{A}$. Similarly the current can be written in terms of a divergence-free (orbital) magnetization by $\mathbf{j}=i\mathbf{q}\times\mathbf{M}$. For convenience, $\mathbf{q}$ is directed along the y axis: $\mathbf{q}=q^y\hat{\mathbf{y}}$. Using the definition of the EM current, and by taking the $q^y\to 0$ limit in this expression, we then obtain $\mathbf{M}(q^y\to 0)=-[P^{xx}(q^y)+n/m]/(q^y)^2|_{q^y\to 0}\mathbf{B}(q^y\to 0)$. From the definition of diamagnetic susceptibility, $\chi_{\rm dia}=-(\partial M^z/\partial B^z)|_{B^z\to 0}$, we then have the following Kubo formula [39]:

$$\chi_{\rm dia}=-\lim_{\mathbf{q}\to 0}\left[\frac{P^{xx}(i\Omega_m=0,\mathbf{q})+n/m}{\mathbf{q}^2}\right]_{q^x=q^z=0}. \tag{3.3}$$

Diamagnetic susceptibility is a transverse response to an applied vector potential; that is, by taking the zero-frequency limit first, and then the momentum limits in the appropriate order, there is no longitudinal contribution to the diamagnetic susceptibility of a uniform Fermi superfluid. Moreover, the Kubo formula in Eq. (3.3) also applies in the condensed phase of a uniform Fermi superfluid. This is because the collective mode contribution to response in a uniform system is purely longitudinal in the zero-frequency, zero-momentum limit, and therefore it gives no contribution to diamagnetic susceptibility. Above the superfluid phase transition temperature, $P^{xx}(0)=-n/m$; this identity enforces the physical constraint that there is no Meissner effect. As a consequence, the Kubo formula can then be written as $\chi_{\rm dia}=-\lim_{\mathbf{q}\to 0}[P^{xx}(i\Omega_m=0,\mathbf{q})-P^{xx}(0)]/\mathbf{q}^2|_{q^x=q^z=0}$.

Another important contribution to magnetic susceptibility is the paramagnetic susceptibility. Paramagnetism is the spin polarization response due to a spin imbalance caused by an external magnetic field. For a system of spin-$\frac{1}{2}$ fermions, the Kubo formula for paramagnetic susceptibility is [32]

$$\chi_{\rm Pauli}=-\lim_{\mathbf{q}\to 0}\mu_{\rm B}^2 P^{00}(i\Omega_m=0,\mathbf{q}), \tag{3.4}$$

where $\mu_{\rm B}$ is the Bohr magneton. In a noninteracting fermionic system, the resulting (Pauli) paramagnetic susceptibility and (Landau) diamagnetic susceptibility satisfy the well-known relation $\chi_{\rm dia}=-\frac{1}{3}\chi_{\rm Pauli}$.

IV. DIAGRAMMATIC ANALYSIS OF RESPONSE FUNCTIONS IN PAIR-FLUCTUATION THEORY

We now build on our discussion in the introduction to incorporate strong-pairing fluctuations. There we motivated a specific choice for the composite boson propagator associated with noncondensed pairs. This is referred to below as the GG_0 pair-fluctuation theory. The self-energy for this theory is

$$\Sigma(k)=\sum_p t(p)G_0(p-k)=\sum_p t(p+k)G_0(p). \tag{4.1}$$

The inverse t matrix is given by $t^{-1}(p)=g^{-1}+\Pi(p)$, with the pair susceptibility $\Pi(p)$ defined by

$$\Pi(p)=\sum_l G_0(p-l)G(l)=\sum_l G(p-l)G_0(l). \tag{4.2}$$

Throughout this paper $k^\mu=(i\omega_n,\mathbf{k})$, $l^\mu=(i\epsilon_n,\mathbf{l})$ denote fermionic four-vectors, while $p^\mu=(i\varpi_m,\mathbf{p})$ and $q^\mu=(i\Omega_m,\mathbf{q})$ denote bosonic four-vectors.

In order to derive the full EM vertex, all bare EM vertex insertions in the self-energy diagram must be performed [38]. After summing all these bare EM vertex insertions, there are in total three possible vertex insertions in the self-energy diagram: (1) a bare EM vertex can be inserted in the bare Green's function $G_0(p-k)$, (2) a full EM vertex can be inserted in the full Green's function in the pair susceptibility $\Pi(p+k)$, and (3) a bare EM vertex can be inserted in the bare Green's function in the pair susceptibility $\Pi(p+k)$. Thus the full EM vertex can be written schematically as

$$\Gamma^\mu_{\rm E}(k_+,k_-)=\gamma^\mu_{\rm E}(k_+,k_-)+{\rm MT}^\mu_{\rm E}(k_+,k_-)+{\rm AL}^\mu_{{\rm E},1}(k_+,k_-)+{\rm AL}^\mu_{{\rm E},2}(k_+,k_-). \tag{4.3}$$

The full EM vertex consists of the bare EM vertex, a Maki-Thompson-like vertex, and two distinct Aslamazov-Larkin-like vertices. These Feynman diagrams are analogous to those in the standard weak-fluctuation theory [5] except that here, as appropriate, there are full rather than bare Green's functions. Note that these vertex corrections appear after making the above diagrammatic insertions: the MT diagram arises from a bare EM vertex insertion in the bare Green's function appearing in the self-energy, while the two AL diagrams enter due to inserting bare or full EM vertices in the appropriate bare or full Green's functions in the pair susceptibility. In Appendix B an explicit derivation of these MT and AL diagrams is presented; their exact forms are given by

$${\rm MT}^\mu_{\rm E}(k_+,k_-)=\sum_p t(p)G_0(p-k_-)\gamma^\mu_{\rm E}(p-k_-,p-k_+)G_0(p-k_+), \tag{4.4}$$

$${\rm AL}^\mu_{{\rm E},1}(k_+,k_-)=-\sum_p\sum_l t(p_-)t(p_+)G_0(p-k)G_0(p-l)G(l_+)\Gamma^\mu_{\rm E}(l_+,l_-)G(l_-), \tag{4.5}$$

$${\rm AL}^\mu_{{\rm E},2}(k_+,k_-)=-\sum_p\sum_l t(p_-)t(p_+)G_0(p-k)G(p-l)G_0(l_+)\gamma^\mu_{\rm E}(l_+,l_-)G_0(l_-). \tag{4.6}$$

One can explicitly check that the full EM vertex satisfies the WTI. To do this, note that the MT and AL diagrams satisfy the following important identity: $q_\mu[2\mathrm{MT}^\mu_{\mathrm{E}}(k_+,k_-)+\mathrm{AL}^\mu_{\mathrm{E},1}(k_+,k_-)+\mathrm{AL}^\mu_{\mathrm{E},2}(k_+,k_-)]=0$. This identity is proved in Appendix B, where it is derived from the definitions of the MT and AL diagrams in Eqs. (4.4)–(4.6). Using this identity, it follows that $q_\mu[\Gamma^\mu_{\mathrm{E}}(k_+,k_-)-\gamma^\mu_{\mathrm{E}}(k_+,k_-)]=-q_\mu\mathrm{MT}^\mu_{\mathrm{E}}(k_+,k_-)$. From the MT vertex given in Eq. (4.4), along with the bare WTI, we then have $q_\mu[\Gamma^\mu_{\mathrm{E}}(k_+,k_-)-\gamma^\mu_{\mathrm{E}}(k_+,k_-)]=\Sigma(k_-)-\Sigma(k_+)$, so that $q_\mu\Gamma^\mu_{\mathrm{E}}(k_+,k_-)=G^{-1}(k_+)-G^{-1}(k_-)$ and thus the full EM vertex satisfies the WTI.

While the formal expression for the full EM vertex can be written down, it is not in closed form due to the fact that this vertex itself appears in the $\mathrm{AL}^\mu_{\mathrm{E},1}$ diagram. We note that the lowest order MT and AL diagrams, which are obtained by setting $\Gamma^\mu_{\mathrm{E}}\to\gamma^\mu_{\mathrm{E}}$, $G\to G_0$, and $t\to t_0$, in Eqs. (4.4)–(4.6), are consistent with those diagrams which have appeared extensively in the weak-fluctuation literature [20,40,41].

The other important contribution to the lowest order EM response functions are the density of states (DOS) diagrams. These diagrams arise from substituting the bare EM vertex part of the full EM vertex into the total response functions. Indeed, the bare EM vertex term in Eq. (4.3) gives a "bubble" contribution to the total response functions in the form $2e^2\sum_k G(k_+)\gamma^\mu_{\mathrm{E}}(k_+,k_-)G(k_-)\gamma^\nu_{\mathrm{E}}(k_-,k_+)$.

By expanding the full Green's functions to second order in Dyson's equation—$G(k)\approx G_0(k)+G_0(k)\Sigma(k)G_0(k)$—the "bubble" contribution becomes $2e^2\sum_k[G_0(k_+)\gamma^\mu(k_+,k_-)G_0(k_-)+G_0(k_+)\gamma^\mu(k_+,k_-)G_0(k_-)\Sigma(k_-)G_0(k_-)+G_0(k_+)\Sigma(k_+)G_0(k_+)\gamma^\mu(k_+,k_-)G_0(k_-)]\gamma^\nu(k_-,k_+)$, which gives the lowest order diagram for noninteracting fermions, plus two additional DOS diagrams. Note that this lowest order set of Feynman diagrams (the noninteracting response plus two DOS, one MT, and two AL diagrams) is not gauge-invariant. These diagrams satisfy the WTI to $O(\Sigma)$, but violate it at $O(\Sigma^2)$. The exact gauge-invariant full EM vertex, which satisfies the WTI, is given in Eqs. (4.3)–(4.6) [42].

For an exact treatment of the EM response, at all temperatures, all diagrams must be considered. In order to make progress in computing the diamagnetic susceptibility for the GG_0 pair-fluctuation theory, certain assumptions must be made and their validity correspondingly needs to be scrutinized. The following sections outline a set of approximations enabling the diamagnetic susceptibility to be calculated analytically. The small parameter controlling these approximations will be discussed in further detail below.

V. APPROXIMATE CALCULATION OF DIAMAGNETIC SUSCEPTIBILITY IN THE SMALL-$|\mu_{\mathrm{pair}}|$ LIMIT

This section derives the diamagnetic susceptibility for the GG_0 pair-fluctuation theory in the fairly extended regime above T_c, where the bosonic chemical potential μ_{pair} is small. The phase transition temperature, T_c, occurs when the pair chemical potential vanishes: $\mu_{\mathrm{pair}}(T_c)=0$. Thus the restriction to the regime where $|\mu_{\mathrm{pair}}|\ll T_c$ is what governs the various approximations made within this calculation. In the typical weak-fluctuation physics [5], this parameter becomes $\epsilon\equiv\ln(T/T_c)\approx(T-T_c)/T_c$. This perturbative regime is necessarily limited to temperatures in close proximity to T_c. By contrast, the constraint associated with the pseudogap state ($|\mu_{\mathrm{pair}}|\ll T_c$) is less restrictive; it is found to apply to considerably higher temperatures, as is discussed in Sec. VII. As a consequence of this result, the temperature range where the diamagnetic susceptibility in the GG_0 pair-fluctuation theory is nearly singular is larger than the corresponding range in the usual weak-fluctuation theory.

It should be noted that near condensation the pair propagator is not so different from a modified free boson propagator, except that there is no fixed number of (composite) boson particles. The propagator depends on the bosonic mass $m_{\mathrm{b}}=M_{\mathrm{pair}}$ and bosonic chemical potential $\mu_{\mathrm{b}}=\mu_{\mathrm{pair}}$, which are determined self-consistently from the underlying fermionic interactions. The pair chemical potential acts as an infrared regulator and the singular nature of the diamagnetic susceptibility is encapsulated by the limit $|\mu_{\mathrm{pair}}|\ll T_c$.

At $q=0$, the full response function satisfies $P^{xx}(0)=-n/m$. To compute the diamagnetic susceptibility from Eq. (3.3), the response function $P^{xx}(0,\mathbf{q})$ must then be expanded to $O(\mathbf{q}^2)$. At all temperatures there will be contributions from the "bubble," Maki-Thompson, and Aslamazov-Larkin diagrams. However, the AL diagrams have one more pair propagator than the MT diagram (without expanding out the full Green's functions or full vertices that is). As discussed in the preceding paragraph, the near-singular nature of the diamagnetic susceptibility arises due to the vanishing of the pair chemical potential. Since the AL diagrams contain one more pair propagator than the MT diagram, the degree of the singularity of the AL contribution to diamagnetic susceptibility (in 3D) is of a higher order than the MT contribution. Indeed, power counting arguments [5,20,21] indicate that near the condensation temperature the AL diagrams give singular contributions to diamagnetic susceptibility, whereas the MT diagram gives a nonsingular diamagnetic response. For this reason, we omit calculating the "bubble" and MT contributions to diamagnetic susceptibility [43]. In the weak-fluctuation theory the contribution to diamagnetic susceptibility from the Aslamazov-Larkin diagrams is also all that needs to be considered [20] near the condensation temperature.

After ignoring the "bubble" and MT contributions, the response function of interest now becomes

$$P^{xx}(0,\mathbf{q})\approx 2e^2\sum_k G(k_+)\big[\mathrm{AL}^x_{\mathrm{E},1}(k_+,k_-)+\mathrm{AL}^x_{\mathrm{E},2}(k_+,k_-)\big]G(k_-)\gamma^x_{\mathrm{E}}(k_-,k_+). \tag{5.1}$$

To contrast the GG_0 pair-fluctuation theory from the weak-fluctuation theory [5,20,41], in Fig. 2 the Aslamazov-Larkin diagrams for both of these theories are shown. Of interest to note is that the weak-fluctuation theory has two identical AL diagrams, containing only bare Green's functions and thus no signature of a normal state pairing gap. In the GG_0 pair-fluctuation theory, however, for the $\mathrm{AL}_{\mathrm{E},1}$ diagram the leftmost triangle vertex contains two full Green's functions and one full EM vertex, while for the $\mathrm{AL}_{\mathrm{E},2}$ diagram this same triangle vertex contains one full Green's function. As a result, the GG_0 pair-fluctuation theory contains dressed Green's functions which depend on the normal state pairing gap.

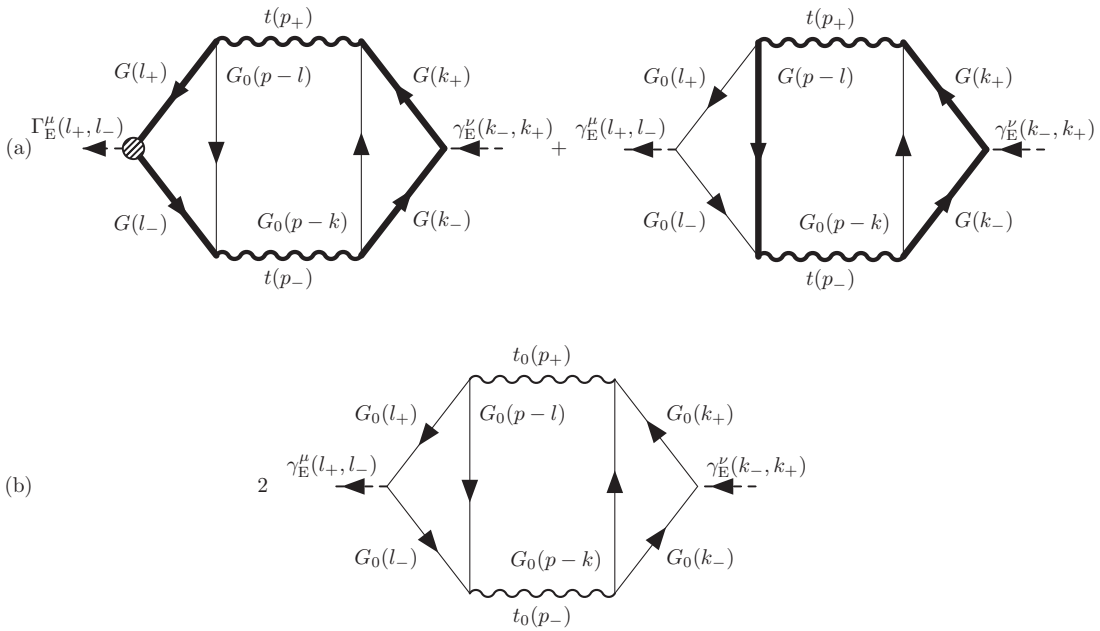

FIG. 2. Comparison of the Aslamazov-Larkin diagrams in (a) GG_0 pair-fluctuation theory and (b) weak-fluctuation theory. These are the dominant diagrams that contribute to diamagnetic susceptibility, near the condensation regime. Of importance is that it is the GG_0 pair-fluctuation theory whose Aslamazov-Larkin diagrams contain full Green's functions depending on the normal state pairing gap, whereas the weak-fluctuation theory contains only bare Green's functions.

The presence of these full Green's functions in the triangle vertex is intimately connected to the form of the t matrix. We emphasize (and discuss in more detail below) that choosing a particular form for the pair-propagator constrains where bare and dressed Green's functions can appear in the Aslamazov-Larkin diagram. All of this is fundamental to the goal of this paper, which is to include pseudogap effects (as incorporated in dressed Green's functions) in a consistent manner in the diamagnetic susceptibility.

Calculating diamagnetic susceptibility requires expanding the response function to $O(\mathbf{q}^2)$, and in the regime where $|\mu_{\rm pair}|$ is small it is only the $\mathbf{q}$ dependence of the pair propagator which is important. As a consequence, we ignore the $\mathbf{q}$ dependence of all the Green's functions appearing in the approximate response function. The remaining $\mathbf{q}$ dependence occurring in $\mathrm{AL}^x_{\mathrm{E},2}(k_+,k_-)$ is then due to the two pair propagators in this vertex. The remaining $\mathbf{q}$ dependence occurring in $\mathrm{AL}^x_{\mathrm{E},1}(k_+,k_-)$ arises from two contributions: the two pair propagators that explicitly appear and the full EM vertex occurring in the leftmost triangle vertex. (See Fig. 2 for reference.)

In expanding the full EM vertex in $\mathrm{AL}^x_{\mathrm{E},1}$ to $O(\mathbf{q}^2)$, we ignore the MT contribution and only expand to quadratic order the $\mathrm{AL}^x_{\mathrm{E},1}$ and $\mathrm{AL}^x_{\mathrm{E},2}$ terms. Thus, all pairs of pair propagators (t matrices) are expanded to quadratic order. Finally, the structure of the $\mathrm{AL}^x_{\mathrm{E},1}$ and $\mathrm{AL}^x_{\mathrm{E},2}$ vertices at $q=0$ is needed. By differentiating the two equivalent expressions for the self-energy appearing in Eq. (4.1) with respect to k^x, the following identities are obtained: $\mathrm{AL}^x_{\mathrm{E},1}(k,k)=\mathrm{AL}^x_{\mathrm{E},2}(k,k)=-\mathrm{MT}^x_{\mathrm{E}}(k,k)$. Therefore, at $q=0$, the full EM vertex is $\Gamma^x_{\mathrm{E}}(k,k)=\gamma^x_{\mathrm{E}}(k,k)+\mathrm{AL}^x_{\mathrm{E},1}(k,k)$.

By iterating this relation in the full EM vertices appearing in $\mathrm{AL}_{\mathrm{E},1}$ and $\mathrm{AL}_{\mathrm{E},2}$ diagrams, and expanding all pairs of t matrices to $O(\mathbf{q}^2)$, the net result is a symmetric product of two bosonic vertices with two pair propagators expanded to quadratic order. The diamagnetic susceptibility thus becomes

$$\chi_{\rm dia}=e^2\sum_p\left[\Lambda^x_{\mathrm{E},1}(p,p)\right]^2\left\{t(p)\frac{\partial^2 t(p)}{\partial(p^y)^2}-\left[\frac{\partial t(p)}{\partial p^y}\right]^2\right\}. \tag{5.2}$$

Here we have defined the bosonic EM vertex $\Lambda^x_{\mathrm{E},1}(p,p)=-\sum_l G_0(p-l)G^2(l)\Gamma^x_{\mathrm{E}}(l,l)$. In this form it is clear that the response function for the AL diagrams reduces to a bosonic response function, with bosonic EM vertices $\Lambda^x_{\mathrm{E},1}(p,p)$ which are modified from a bosonic bare EM vertex due to the underlying fermionic interactions.

Using the WTI the bosonic EM vertex $\Lambda^x_{\mathrm{E},1}(p,p)$ can be written in terms of derivatives of the pair susceptibility $\Pi(p)$ as

$$\frac{\partial\Pi(p)}{\partial p^x}=\sum_l G_0(p-l)G^2(l)\Gamma^x(l,l)=-\Lambda^x_{\mathrm{E},1}(p,p). \tag{5.3}$$

An equivalent expression is $\Lambda^x_{\mathrm{E},1}(p,p)=-\sum_l G(p-l)G_0^2(l)\gamma^x(l,l)=\Lambda^x_{\mathrm{E},2}(p,p)$. Further details on this derivation are given in Appendix E2. Inserting this result into Eq. (5.2) then gives the diamagnetic susceptibility as

$$\chi_{\rm dia}=e^2\sum_p\left[\frac{\partial\Pi(p)}{\partial p^x}\right]^2\left\{t(p)\frac{\partial^2 t(p)}{\partial(p^y)^2}-\left[\frac{\partial t(p)}{\partial p^y}\right]^2\right\}. \tag{5.4}$$

In the small-$|\mu_{\rm pair}|$ limit, when performing the Matsubara frequency summation only the lowest order term in the frequency integral with bosonic frequency equal to zero needs to be retained [20]. In Appendix C, the Matsubara frequency summation is carried out analytically and the preceding assumption

is validated. Thus, we now have

$$\chi_{\rm dia} = Te^2 \sum_{\mathbf{p}} \left[\frac{\partial \Pi(\mathbf{p})}{\partial p^x}\right]^2 \left\{ t(\mathbf{p}) \frac{\partial^2 t(\mathbf{p})}{\partial (p^y)^2} - \left[\frac{\partial t(\mathbf{p})}{\partial p^y}\right]^2 \right\}. \quad (5.5)$$

Here $\Pi(\mathbf{p}) \equiv \Pi(0,\mathbf{p})$ and $t(\mathbf{p}) \equiv t(0,\mathbf{p})$. To evaluate the form of the vertices involving the derivatives of the susceptibility, we use the definition $t^{-1}(p) = g^{-1} + \Pi(p)$, along with the approximate form of the pair propagator given in Eq. (1.1), to obtain $\partial\Pi(\mathbf{p})/\partial p^x = \partial t^{-1}(p)/\partial p^x = -Zp^x/M_{\rm pair}$. The result for the bosonic EM vertex $\Lambda^x_{\mathrm{E},1}$ is of the same form as one would expect for actual bosons, but with a modified mass.

We emphasize again that the composite boson EM vertex appearing in the diamagnetic susceptibility is tightly constrained by the form of the t matrix. Thus, one cannot assume a fixed form for the pair propagator, and then modify the Green's functions in the triangle vertex appearing in the AL diagram [28], without also modifying the pair propagator.

Using the form of the bosonic EM vertex computed above, along with the approximate form of the t matrix in Eq. (1.1), and after performing integration by parts, the diamagnetic susceptibility reduces to

$$\begin{aligned}\chi_{\rm dia} &= \frac{2Te^2}{3M_{\rm pair}} \sum_{\mathbf{p}} \left(\frac{p^x}{M_{\rm pair}}\right)^2 [Zt(0,\mathbf{p})]^3 \\ &= -\frac{4Te^2}{9\pi^2} \int_{-\infty}^{\infty} dp\, \frac{p^4}{(p^2 + 2M_{\rm pair}|\mu_{\rm pair}|)^3}. \end{aligned} \quad (5.6)$$

Note that $\mu_{\rm pair} = -|\mu_{\rm pair}|$ is negative, while $M_{\rm pair}$ is positive; this allows the spatial integral in the above expression to be computed. The p integration is easily performed using a closed contour integration in the upper half plane and evaluating the residue at the pole $p = i(2M_{\rm pair}|\mu_{\rm pair}|)^{1/2}$. This gives the result presented in Eq. (1.2) above:

$$\chi_{\rm dia} = -\frac{k_B T (2e)^2}{24\pi\hbar c^2} \sqrt{\frac{1/(2M_{\rm pair})}{|\mu_{\rm pair}|}}. \quad (5.7)$$

Here the constants $\hbar$, k_B, and c have been restored to ensure that $\chi_{\rm dia}$ is dimensionless. The diamagnetic susceptibility has been written in this form to allow direct comparison with free bosonic transport. In Appendix D it is shown that, for free bosons, the diamagnetic susceptibility in the small chemical potential limit is $\chi_{\rm b} = -\frac{k_B T (e^*)^2}{24\pi\hbar c^2} \sqrt{\frac{1/(2m_{\rm b})}{|\mu_{\rm b}|}}$. Thus, in the small-$|\mu_{\rm pair}|$ limit the diamagnetic susceptibility for the GG_0 pair-fluctuation theory behaves like free bosons, but with effective charge $e^* = 2e$, mass $m_{\rm b} = M_{\rm pair}$, and chemical potential $\mu_{\rm b} = \mu_{\rm pair}$. The factor of 2 in the charge reflects the underlying internal fermionic constituents of these composite bosons.

VI. THERMOELECTRIC RESPONSE

In this section we investigate thermoelectric response and the Nernst coefficient in the presence of a normal state pseudogap. Here we follow the framework introduced in the previous sections in the analysis of the diamagnetic susceptibility. In contrast to the rather precise statements that were made about diamagnetic susceptibility in the pseudogap regime, for the Nernst response the situation is far more complex. Indeed, there is extensive controversy in the literature about this response function, even in the weak-fluctuation limit [21,44–46]. There have also been attempts to study this quantity beyond the weak-fluctuation limit [23,28,30]. To make progress, it will be useful to build on the more detailed and solid understanding of diamagnetic susceptibility presented in the preceding sections. By again focusing on the central bosonic physics it is possible to express the Nernst coefficient in terms of bosonic response functions, with the parameters $\mu_{\rm pair}$ and $M_{\rm pair}$ encapsulating pseudogap effects. The Nernst response in the weak-fluctuation limit will serve as a point of comparison.

The Nernst coefficient arises in transport by applying a temperature gradient $(-\nabla T)_x$ in the presence of a magnetic field $\mathbf{B} = B\hat{\mathbf{z}}$ and subsequently measuring the electric field response $\mathbf{E} = E\hat{\mathbf{y}}$ (in the absence of a transport electric current). This transport coefficient is defined by [21]

$$\nu_N = \frac{E}{(-\nabla T)_x B} = \frac{1}{B} \frac{\alpha_{xy}\sigma_{xx} - \alpha_{xx}\sigma_{xy}}{\sigma_{xx}^2 + \sigma_{xy}^2}. \quad (6.1)$$

For a particle-hole symmetric system (defined to mean a constant density of states near the Fermi surface), $\sigma_{xy} = 0$, so that $\nu_N = \alpha_{xy}/(B\sigma_{xx})$. The Nernst coefficient is then reduced to calculating the transverse thermoelectric coefficient α_{xy} and electrical conductivity σ_{xx}. For the GG_0 pair-fluctuation theory there is no particle-hole symmetry except in the BCS regime. Nevertheless, here we study only α_{xy} as an indication of the more complicated Nernst coefficient.

The Kubo formalism for thermal response is not as straightforward as it is for electric response. Indeed, the formulation of equilibrium linear response to a temperature change causes conceptual difficulties [32]. One issue is that there is no unique definition of the heat-current vertex. Formally, the flow of heat corresponds to the flow of energy in the absence of the flow of matter [32,33]. The heat current is thus equivalent to the energy current, and to derive the form of the heat vertex we must investigate the consequences of energy conservation. As discussed in Sec. III, the global U(1) particle number symmetry leads to a corresponding WTI. The same is true for energy conservation. Indeed, this conservation law arises from the invariance of the Lagrangian of a theory under time translations. The corresponding WTI, which reflects the law of conservation of energy in terms of Green's functions, is [47]

$$q_\mu \Gamma^\mu_{\rm H}(k_+,k_-) = \omega_- G^{-1}(k_+) - \omega_+ G^{-1}(k_-), \quad (6.2)$$

where $\omega_\pm \equiv \omega \pm \Omega/2$. Here $\Gamma^\mu_{\rm H}$ is the full heat vertex. This form of the WTI is not unique, and alternative forms can be derived by using the equations of motion; for further details see Ref. [47]. The bare WTI for energy conservation, $q_\mu \gamma^\mu_{\rm H}(k_+,k_-) = \omega_- G_0^{-1}(k_+) - \omega_+ G_0^{-1}(k_-)$, is satisfied by the bare heat vertex $\gamma^\mu_{\rm H}(k_+,k_-) = (\gamma^0_{\rm H}(k_+,k_-), \gamma^i_{\rm H}(k_+,k_-))$, where $\gamma^0_{\rm H}(k_+,k_-) = (\mathbf{k}_+ \cdot \mathbf{k}_-)/2m - \mu$ and $\gamma^i_{\rm H}(k_+,k_-) = [\omega_+ k^i_- + \omega_- k^i_+]/(2m)$. The bare heat vertex $\gamma^i_{\rm H}(k+q,k) = [i\omega_n(k^i + q^i) + (i\omega_n + i\Omega_m)k^i]/(2m)$ agrees with Ref. [33].

As in Sec. IV, the full heat vertex is found by performing all possible bare heat vertex insertions in the self-energy diagram. However, an additional vertex insertion arises from

inserting the energy-momentum tensor interaction directly into the t matrix. The final result is that the full heat vertex is

$$\Gamma^{\mu}_{\rm H}(k_+,k_-) = \gamma^{\mu}_{\rm H}(k_+,k_-) + {\rm MT}^{\mu}_{\rm H}(k_+,k_-) + \lambda^{\mu}_{\rm H}(k_+,k_-) + {\rm AL}^{\mu}_{\rm H,1}(k_+,k_-) + {\rm AL}^{\mu}_{\rm H,2}(k_+,k_-). \tag{6.3}$$

The Maki-Thompson, Aslamazov-Larkin, and $\lambda^{\mu}_{\rm H}$ heat-current vertices are

$${\rm MT}^{\mu}_{\rm H}(k_+,k_-) = \sum_p t(p)G_0(p-k_-)\gamma^{\mu}_{\rm H}(p-k_-,p-k_+)G_0(p-k_+), \tag{6.4}$$

$${\rm AL}^{\mu}_{\rm H,1}(k_+,k_-) = -\sum_p\sum_l t(p^-)t(p^+)G_0(p-k)G_0(p-l)G(l^+)\Gamma^{\mu}_{\rm H}(l^+,l^-)G(l^-), \tag{6.5}$$

$${\rm AL}^{\mu}_{\rm H,2}(k_+,k_-) = -\sum_p\sum_l t(p^-)t(p^+)G_0(p-k)G(p-l)G_0(l^+)\gamma^{\mu}_{\rm H}(l^+,l^-)G_0(l^-), \tag{6.6}$$

$$\lambda^{\mu}_{\rm H}(k_+,k_-) = \sum_p g^{-1}\delta^{\mu 0}t(p^+)t(p^-)G_0(p-k_+). \tag{6.7}$$

Here $\delta^{\mu 0}$ is the Kronecker delta function, equal to unity only for the time component ($\mu = 0$) and zero otherwise. In Appendix E1 an explicit calculation is presented which shows that the full heat vertex, as determined by Eqs. (6.3)–(6.7), satisfies the WTI in Eq. (6.2).

Following Ref. [21], we consider the heat-current response to an applied electric field. The applied electric and magnetic fields are in the $\hat{x}$ and $\hat{z}$ directions, respectively, and the heat-current response is considered in the $\hat{y}$ direction. The correlation function of interest is then a heat current–electric current correlation function: $P^{yx}_{\rm HE}(i\Omega_m,\mathbf{0}) = 2e\sum_k G(k_+)\Gamma^{y}_{\rm H}(k_+,k_-)G(k_-)\gamma^{x}_{\rm E}(k_-,k_+)$, where $\mathbf{q} = 0$. The full heat vertex is determined in Eqs. (6.3)–(6.7), and since only the $\hat{y}$ component is of interest, the vertex in Eq. (6.7) gives zero contribution.

Here we calculate the transverse thermoelectric coefficient only to linear order in magnetic field. This linearization results in performing all possible ($\hat{y}$ component) electromagnetic vertex insertions in the heat current–electric current correlation function [48]. The resulting correlation function is a three-point correlation function: $\Lambda^{yyx}(i\Omega_m,Q)$, where $\mathbf{Q} = Q\hat{\mathbf{x}}$ represents the momentum inserted into the heat current–electric current correlation function. The transverse thermoelectric response, $\widetilde{\alpha}_{xy}$, can then be computed to linear order in magnetic field B using the definition $\widetilde{\alpha}_{xy} = B[c\chi_{\rm dia}/\hbar - j_y/(EB)]$, where the second term is determined from the Kubo formula [21]:

$$\frac{j_y}{EB} = -\lim_{\Omega,Q\to 0}\frac{1}{\Omega Q c}{\rm Re}[\Lambda^{yyx}(\Omega,Q)|_{i\Omega_m\to\Omega+i0^+}]. \tag{6.8}$$

The order of limits is crucial: first $Q\to 0$, and then $\Omega\to 0$. The need for including the magnetization current in the above definition [49] is because they contribute to the total microscopic current, and therefore must be subtracted to obtain the transport current [21]. The parameter α_{xy} appearing in the Nernst coefficient is then determined by $\alpha_{xy} = \widetilde{\alpha}_{xy}/T$.

The total number of EM vertex insertions is quite formidable, and an exact theoretical treatment is challenging. In principle, if one inserts the full EM vertex into all the full Green's functions, the bare EM vertex into all the bare Green's functions, and the appropriate triangle vertices into all the t matrices appearing in $P^{yx}_{\rm HE}(i\Omega_m,\mathbf{0})$, then the full set of Feynman diagrams for the heat-current response to an applied electric and magnetic field will be obtained. For the GG_0 pair-correlation theory in particular, the various full Green's functions and full vertices present in the response function means there will be a large number of diagrams to consider, more so than in the weak-fluctuation case.

However, on the basis of the analysis performed in the previous section, and also from the near-condensation calculations for the weak-fluctuation theory [21], it is expected that only the AL diagrams with EM vertices inserted into the t matrix give singular contributions. This is because such diagrams contain three t-matrix propagators, and thus in the small-$|\mu_{\rm pair}|$ limit they have a higher order in their degree of singularity than any other diagrams. See Ref. [21] for the subtleties involved in the power counting arguments related to the Nernst response.

Therefore, as an approximate calculation, we consider only the EM vertex insertions in the t matrices appearing in the two AL diagrams that contribute to the heat current–electric current correlation function. There are two EM triangle vertices that can be inserted into each of the t matrices appearing in both ${\rm AL}_{\rm H,1}$ and ${\rm AL}_{\rm H,2}$. These arise from the GG_0 Green's functions appearing in the pair susceptibility, and thus either the full or bare EM vertex can be inserted into the corresponding Green's function, which results in the two different types of EM triangle vertices.

Since the bosonic EM vertex $\Lambda_{\rm E,1} = \Lambda_{\rm E,2}$ is the same for both EM triangle vertices appearing in ${\rm AL}_{\rm E,1}$ and ${\rm AL}_{\rm E,2}$ diagrams, this results in a symmetry factor of two. (For further details see Appendix E2.) In addition there is another factor of two due to spin degeneracy for a system of spin-$\frac{1}{2}$ fermions. Thus, the Nernst calculation is effectively reduced to calculating two AL diagrams, plus their mirror images, with one corresponding bosonic heat vertex ($\Lambda^{y}_{\rm H,1}$ or $\Lambda^{y}_{\rm H,2}$ depending on the diagram) and two bosonic EM vertices ($\Lambda^{y}_{\rm E,1}$, $\Lambda^{x}_{\rm E,1}$), multiplied by a symmetry factor of four.

There is extensive debate in the literature about the correct gauge-invariant approach to heat response [45,50]. Part of the issue concerns the appropriate diagrams to include, and how to ensure that gauge invariance is satisfied. For further discussion see also Refs. [51–53]. Here we note that the full heat vertex presented in Eqs. (6.3)–(6.7) is consistent with the WTI for energy conservation in Eq. (6.2).

Another issue under debate is the role of particle-hole asymmetry. In Ref. [45] it is claimed that the Nernst

response vanishes without particle-hole asymmetry. However, in Ref. [54] this claim is refuted. Indeed, for a normal Fermi metal that possesses particle-hole symmetry the Nernst coefficient is (approximately) zero [46,51,54]. In the weak-fluctuation case, however, the bosonic contribution to Nernst response from the AL diagrams is found to be significant [21,46,51], even in the absence of particle-hole asymmetry.

There is also contention in the Nernst literature [21,28,44–46] concerning the specific form of the heat vertex appearing in the AL diagrams. This uncertainty is in contrast to the bosonic EM vertex, given in Eq. (5.3). Following the EM vertex calculation, a similar analysis can be performed for the heat vertex. Since it is more involved, the derivation is presented in Appendix E3. The result is that the sum of the heat triangle vertices for $\mathrm{AL}^y_{\mathrm{H},1}$ and $\mathrm{AL}^y_{\mathrm{H},2}$ reduces to a bosonic heat vertex, defined by $\Lambda^y_{\mathrm{H},1}(p,p)+\Lambda^y_{\mathrm{H},2}(p,p)\equiv\Lambda^y_{\mathrm{H}}(p,p)=-\varpi[\partial t^{-1}(p)/\partial p^x]$.

For comparison, the fermionic heat vertex obeys $\Gamma^y_{\mathrm{H}}(k,k)=-\omega[\partial G^{-1}(k)/\partial k^x]$. Note, there is an additional factor of two compared to the EM case, which obeys $\Lambda^y_{\mathrm{E},1}(p,p)+\Lambda^y_{\mathrm{E},2}(p,p)\equiv\Lambda^y_{\mathrm{E}}(p,p)=2[\partial t^{-1}(p)/\partial p^y]$. The Nernst literature [21,28,44–46] debates this factor of two; in Appendix E3 we provide our own interpretation which makes the result less ambiguous. The point is that the heat and EM vertices, for fermions and bosons, are related by $\Gamma^y_{\mathrm{H}}(k,k)=(\omega/e)\Gamma^y_{\mathrm{E}}(k,k)$ and $\Lambda^y_{\mathrm{H}}(p,p)=(\varpi/e^*)\Lambda^y_{\mathrm{E}}(p,p)$, where $e^*=2e$ [37]. Independent work [55] has also arrived at the same conclusion, based on a similar derivation using the Ward-Takahashi identity.

Now we return to the calculation of the transverse thermoelectric coefficient. The previous analysis of the heat vertex means that the Nernst response is reduced to calculating one Aslamazov-Larkin diagram, plus its mirror image, with one bosonic heat vertex (Λ^y_{H}) and two bosonic EM vertices ($\Lambda^y_{\mathrm{E},1},\Lambda^x_{\mathrm{E},1}$), multiplied by a symmetry factor of four. It is important to note that in combining the two heat vertices $\Lambda^y_{\mathrm{H},1}$ and $\Lambda^y_{\mathrm{H},2}$ into one bosonic heat vertex Λ^y_{H} the number of diagrams that need to be computed has effectively been reduced by a factor of two. Thus, the three-point correlation function that needs to be computed is

$$\Lambda^{yyx}(i\Omega_m,Q)=-4e^2\sum_p\Bigg[\frac{Zp^x_+}{M_{\mathrm{pair}}}\left(\frac{Zp^y}{M_{\mathrm{pair}}}\right)^2(i\varpi_m+i\Omega_m/2)t(i\varpi_m+i\Omega_m/2,\mathbf{p}_+)t(i\varpi_m,\mathbf{p}_-)t(i\varpi_m,\mathbf{p}_+)$$
$$+\frac{Zp^x_-}{M_{\mathrm{pair}}}\left(\frac{Zp^y}{M_{\mathrm{pair}}}\right)^2(i\varpi_m-i\Omega_m/2)t(i\varpi_m-i\Omega_m/2,\mathbf{p}_-)t(i\varpi_m,\mathbf{p}_+)t(i\varpi_m,\mathbf{p}_-)\Bigg],\tag{6.9}$$

where $\mathbf{p}_\pm\equiv\mathbf{p}\pm\mathbf{Q}/2$.

Performing the Matsubara frequency summation, and then taking the limits $Q\to0$, followed by $\Omega\to0$ in the Kubo formula given in Eq. (6.8), we obtain

$$\frac{j_y}{EB}=-\frac{k_BTe^2}{4\pi\hbar^2c}\sqrt{\frac{1/(2M_{\mathrm{pair}})}{|\mu_{\mathrm{pair}}|}}\left(\frac{\kappa^2+\Gamma^2}{\Gamma^2}\right).\tag{6.10}$$

Here the constants $\hbar$, k_B, and c have been restored. For further details of the calculation see Appendix E4. The transverse thermoelectric coefficient, $\widetilde{\alpha}_{xy}$, is then found by combining Eqs. (5.7) and (6.10) and using the definition $\widetilde{\alpha}_{xy}=B[c\chi_{\mathrm{dia}}/\hbar-j^y/(EB)]$; this gives the result stated in Eq. (1.3) at the beginning of the paper:

$$\widetilde{\alpha}_{xy}=\frac{Bk_BTe^2}{12\pi\hbar^2c}\sqrt{\frac{1/(2M_{\mathrm{pair}})}{|\mu_{\mathrm{pair}}|}}\left(\frac{3\kappa^2+\Gamma^2}{\Gamma^2}\right).\tag{6.11}$$

Similar results can be obtained from Ref. [30]. Just as for the diamagnetic susceptibility, the transverse thermoelectric coefficient in Eq. (6.11) is large when $|\mu_{\mathrm{pair}}|\ll T_c$. In the $\kappa\to0$ limit, Eq. (6.11) reproduces the result in the weak-fluctuation literature [21]. It is of interest to note that whereas diamagnetic susceptibility is insensitive to the parameter Γ, the transverse thermoelectric coefficient depends crucially on this parameter. The parameter Γ serves as a regularization for the transverse thermoelectric coefficient in the BEC limit, whereas for diamagnetic susceptibility such a regularization is not required.

The ratio of the absolute magnetization to the transverse thermoelectric coefficient has received a lot of interest [23]; in the weak-fluctuation limit this ratio is exactly $2(\hbar/c)$: $|Bc\chi_{\mathrm{dia}}|/(\hbar\widetilde{\alpha}_{xy})=2$, and in the phase-only fluctuation picture this ratio is obtained in the large-temperature limit [23]. From the results in Eqs. (5.7) and (6.11), we find this ratio to be $|Bc\chi_{\mathrm{dia}}|/(\hbar\widetilde{\alpha}_{xy})=2[1-3\kappa^2/(3\kappa^2+\Gamma^2)]$. In the weak-fluctuation limit $\kappa=0$, and we recover the standard result. More generally, the BCS limit is $\Gamma\gg\kappa$, so that $|Bc\chi_{\mathrm{dia}}|/(\hbar\widetilde{\alpha}_{xy})\to2$; however, the BEC limit is $\Gamma\ll\kappa$, so that $|Bc\chi_{\mathrm{dia}}|/(\hbar\widetilde{\alpha}_{xy})\to(2/3)(\Gamma/\kappa)^2$. In the intermediate pseudogap regime, where both $\kappa,\Gamma\neq0$, the ratio is in between these two limits; it decreases as the pairing strength increases.

In summary, the singular nature of the diamagnetic susceptibility and transverse thermoelectric coefficient shows the importance of including fluctuating bosonic degrees of freedom. The next section presents numerical results for the diamagnetic susceptibility, which depends on the effects of the normal state gap through the parameters M_{pair} and μ_{pair}.

VII. NUMERICAL RESULTS

We now present the results of our numerical calculations of the cuprate diamagnetic susceptibility, along with a comparison to experimental data. To compare between theory and experiment, it is first necessary to start with a semiquantitative understanding of the phase diagram. Section II outlined a procedure to compute both T_c and T^* using the t matrix of Eq. (2.4). The resulting phase diagram is shown in Fig. 3, which plots both T_c (blue) and T^* (red) curves as functions of doping concentration, x. Qualitatively the horizontal axis is a measure of the dimensionless interaction strength with stronger

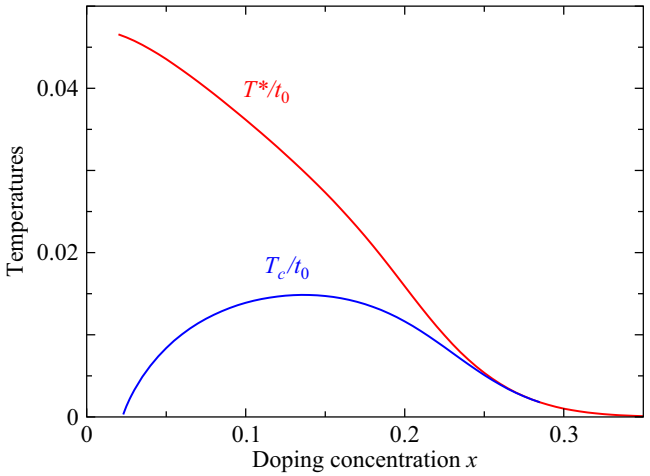

FIG. 3. Theoretically calculated cuprate phase diagram. Plotted are T_c and T^*, in units of t_0, as functions of doping concentration x.

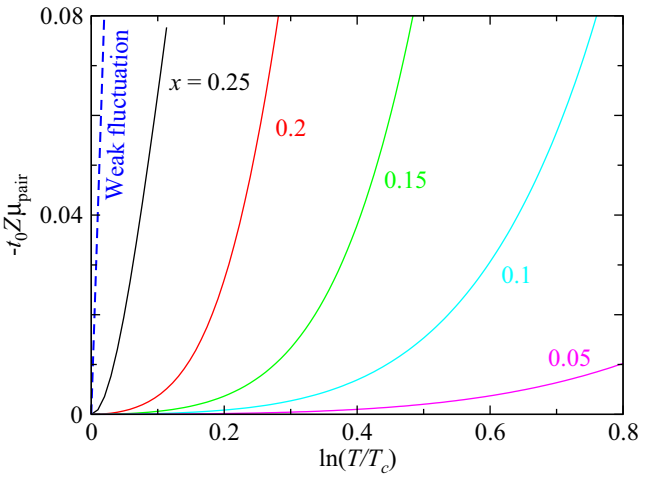

FIG. 4. The product $-t_0 Z\mu_{\rm pair}$ as a function of $\epsilon = \ln(T/T_c)$ for various doping concentrations x from overdoped ($x = 0.25$) to underdoped ($x = 0.05$). For comparison, the result from the weak-fluctuation formalism (blue dashed straight line) is also plotted.

(weaker) interaction effects on the left (right) side, reflecting underdoped (overdoped) cuprates. This figure generically indicates what occurs in the weak-interaction regime (on the right), where $T_c \approx T^*$, and the strong-interaction regime (on the left), where T_c and T^* are anticorrelated.

This anticorrelation can be understood from the early work of Nozières and Schmitt-Rink [56] who showed that, on a lattice, as the attraction becomes stronger it becomes increasingly difficult for pairs to hop, since they first need to unbind. This is responsible for the large pair mass. In the d-wave case the effects are more extreme [8] as the pairs are more extended in size. At sufficiently strong attraction a superconductor-insulator transition is observed. This explains the behavior at the lower critical doping of the T_c dome.

The phase diagram in Fig. 3 is based on a nearest-neighbor quasi-two-dimensional tight-binding band structure. The cuprate half bandwidth $4t$ for the in-plane dispersion sets the scale for the units of energy. The anisotropy parameter is taken as $t_z/t = 0.003$, in agreement with estimates for BSCCO and LSCO superconductors. Note that the T_c curve depends on t_z/t only logarithmically. Details of the band parameters are not particularly important, provided they are chosen to capture the generic effect that T^* increases with under doping. Our calculations have included the doping concentration x and *doping-independent* interaction strength g. The x dependence is included in the hopping integral t in the form $t \approx t_0 x$, where t_0 is an energy scale characteristic of the parent compound. We choose the dimensionless ratio $-g/4t_0 = 0.04725$ to optimize the fit to T^*. For the moment only the single parameter t_0 is left unspecified.

The plot in Fig. 3 shows that T_c vanishes at a lower critical doping of $x = 0.025$, which is slightly less than the experimental value of $x = 0.05$ [7]. Nevertheless the overall shape as compared with experiment, shown below in Fig. 6, for T_c (and T^*), is reasonable. While not shown in Fig. 3, at each value of x the magnitude of the pairing gap Δ (or pseudogap), at T_c for example, shows an approximate proportionality to T^*.

The diamagnetic susceptibility has a singular inverse square root dependence on the bosonic chemical potential, $\mu_{\rm pair}$, as derived in Eq. (5.7). This pair chemical potential itself varies with temperature and doping concentration. It is useful, then, to first study $\mu_{\rm pair}$ and compare with the weak-fluctuation limit. The combination $-Z\mu_{\rm pair}$ in the strong-pairing theory can be viewed as equivalent to $N_0\epsilon$ in the weak-fluctuation theory, where N_0 is the fermionic density of states at the Fermi surface and $\epsilon = \ln(T/T_c)$. The parameter Z, which is the prefactor of proportionality in the t matrix defined in Eq. (1.1), is associated with the linear frequency contribution to the inverse t matrix.

In Fig. 4 we plot the product $-t_0 Z\mu_{\rm pair}$, as a function of $\ln(T/T_c)$, for different doping concentrations as labeled, from the overdoped ($x = 0.25$) to the strongly underdoped ($x = 0.05$) limit. The blue dashed straight line is $N_0\epsilon$ in the weak-fluctuation theory. To make this comparison we have estimated the fermion mass on a quasi-2D lattice at the Fermi level using an in-plane Fermi wave vector $\mathbf{k} = 0.9(\pi/2,\pi/2)$ along the nodal direction, which yields an effective fermion mass $m = 1/(0.31t)$. This leads to the association $t_0 N_0 = t_0(m/\pi) = 4.1$ (for $x = 0.25$), which sets the slope of the blue dashed line.

It is evident from Fig. 4 that, as the magnitude of the pseudogap increases from the overdoped to underdoped regime, $-t_0 Z\mu_{\rm pair}$ decreases rapidly for a given ϵ. This means that in the underdoped regime there is a larger range of temperatures where $|\mu_{\rm pair}|$ is effectively "small." As a consequence, the strong-pairing fluctuation theory has a large diamagnetic susceptibility at temperatures higher than is the case for the diffusive, weak-fluctuation theory.

Now we are in a position to study the behavior of the normal state diamagnetic susceptibility. In order to calculate $\chi_{\rm dia}$ for the quasi-2D cuprates, in an extended range of temperatures above T_c, we use Eq. (5.4) supplemented by Eq. (D9) in Appendix D, with $e^* = 2e$, $m_{\rm b}$ replaced by the in-plane pair mass $M_\parallel$, and $\xi_{\mathbf{p}}$ replaced by the appropriate anisotropic pair dispersion $\Omega_{\mathbf{p}}$ [31]. Of particular importance is the onset temperature [7], T_χ. This is the temperature at which the total magnetic susceptibility departs from the background contribution. We consider the background contribution to the total magnetic susceptibility as arising from the (Pauli) paramagnetic [57] contribution, $\chi_{\rm Pauli}$, associated with the

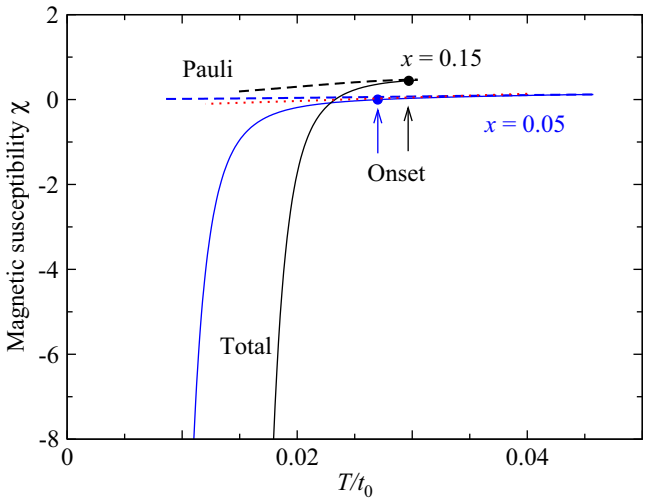

FIG. 5. Magnetic susceptibility above T_c at optimal doping $x = 0.15$ (black) and underdoping $x = 0.05$ (blue). The dashed lines are the Pauli paramagnetic susceptibility and the solid lines are the sum of the paramagnetic and diamagnetic contributions to magnetic susceptibility. The solid dots indicate the temperature, T_χ, at which the onset of diamagnetic susceptibility occurs. For the underdoped case, the red dotted line is a linear fit to the high-temperature data.

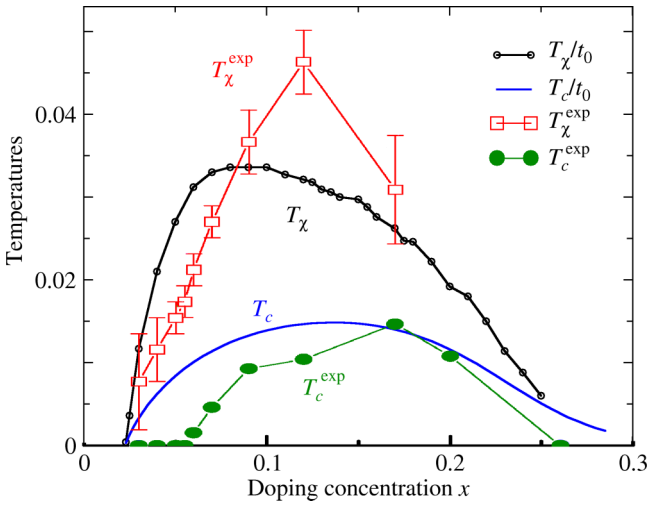

FIG. 6. Doping dependence of the calculated diamagnetic susceptibility onset temperature T_χ (black) and T_c (blue), along with corresponding experimental data from Ref. [7] for T_χ (red squares) and T_c (green discs). For both cases, the maximum of T_χ is skewed towards the underdoped regime.

fermionic quasiparticles. The crucial contribution in this analysis is the diamagnetic susceptibility, $\chi_{\rm dia}$, which is dominated by the bosonic pairing fluctuations. The total magnetic susceptibility is then $\chi = \chi_{\rm Pauli} + \chi_{\rm dia}$.

From a theoretical point of view it is reasonable to view the dominant background contribution to be based on $\chi_{\rm Pauli}$. The experimental background [7], however, indicates that the Pauli contribution is relatively insignificant compared to a much larger Van Vleck paramagnetic term, $\chi_{\rm VV}$. This Van Vleck contribution is difficult to theoretically calculate from first principles. The experimental data suggests that $\chi_{\rm VV}$ is approximately 1–2 orders of magnitude larger than $\chi_{\rm Pauli}$. Accordingly we adjust the vertical scale of our total magnetic susceptibility to give an analogous effect to the experimentally measured background term.

In Fig. 5 we indicate this procedure. We focus on two representative examples for the optimal doping case $x = 0.15$ (black curves) and the underdoped case $x = 0.05$ (blue curves) to illustrate how the diamagnetic onset temperatures are determined. This onset is indicated in the figure by the colored dot. For the former case, the onset is simply given by the departure temperature of the total susceptibility (solid curve) from the Pauli background (dashed curve). For the strongly underdoped (blue curve) case, there is a large temperature regime above T_χ where $\chi_{\rm dia}$ is small but nonzero. In such cases, for example $x = 0.05$, we closely follow the experimental procedure by fitting χ in this regime with a (red dotted) straight line and then determine T_χ by where χ departs from this line.

Summarizing our results, the extracted diamagnetic susceptibility onset temperature, T_χ, is plotted in Fig. 6 as the open black circles, while the experimental data from Ref. [7] is shown in the open red squares. The theoretical and experimental transition temperatures are also plotted. We determine the previously unspecified energy scale t_0 by fitting the theoretical T_c curve to the experimentally measured T_c near optimal doping ($x = 0.15$).

Our theoretically calculated diamagnetic susceptibility onset temperatures are found to be in reasonable agreement with the experimental data in the underdoped and overdoped cases. The theoretical plot has a peak in T_χ which is skew-symmetric towards the underdoped regime; this is a feature also exhibited in the experimental data. The experimentally observed decrease in T_χ in the underdoped regime is a feature which is captured in the theoretical plot. This is an important theoretical finding because this regime is outside the applicability of the weak-fluctuation theory. The theoretical T_χ vanishes simultaneously with T_c as the doping concentration approaches its lower critical value [58].

The peak in T_χ in the experimental data is, however, slightly higher than the peak in the theoretically predicted values. More experimental data and a better theoretical treatment of the background contribution would aid in this regard. Nonetheless, the prediction that there is a significant high-temperature contribution to diamagnetic susceptibility due to strong pair fluctuations, as expressed in Eq. (5.7), is captured in the theoretical figures.

While a comparison between the theoretical and experimental Nernst coefficient has not been presented, it should be pointed out that the onset temperature of the transverse thermoelectric response is expected to be roughly the same as T_χ. This follows from the simple proportionality between absolute magnetization and transverse thermoelectric coefficient: $\propto 2\Gamma^2/(3\kappa^2 + \Gamma^2)$. We note that the parameters κ and Γ are weakly temperature dependent, so that T_χ is a reasonable estimate for this thermoelectric onset temperature. This observation appears consistent with experimental claims in Ref. [7].

VIII. CONCLUSIONS

In this paper we have studied the effects of a normal state pseudogap on the diamagnetic susceptibility and transverse

thermoelectric coefficient, as applied to the hole-doped cuprates. Strong support for a cuprate pseudogap deriving from a "preformed-pair" scenario comes from the anomalous enhancement in both these quantities. An essential addition to the literature then is a calculation of these transport coefficients, which incorporates into the underlying response theory the presence of a pseudogap itself. This paper achieves this goal, by using a strong-pairing fluctuation theory in which the dominant contributions to the diamagnetic susceptibility and transverse thermoelectric coefficient come from modified Aslamazov-Larkin diagrams. This differs from the conventional weak-pairing fluctuation theory in which these two transport coefficients were derived in the absence of a normal state gap. By incorporating longer-lived and more stable fermion pairs, we find our calculations compare favorably with their experimental counterparts over the broad range of hole-doping concentrations.

These results are obtained through detailed diagrammatic calculations which are tightly constrained by the Ward-Takahashi identity. They depend importantly on the associated form of the pair propagator, which differs from its weak-fluctuation analog in large part because the pairs have propagating rather than diffusive dynamics. We have emphasized in this paper that the calculation related to the thermoelectric coefficient is not at the same level of rigor as that for diamagnetic susceptibility, which from our perspective is quite precise. Nevertheless there is a fair degree of confidence that, just as for the diamagnetic susceptibility, the important parameter controlling the singular behavior in the transverse thermoelectric coefficient is of the form $\sqrt{1/(2M_{\rm pair}|\mu_{\rm pair}|)}$.

More generally we note the similarity between the transverse thermoelectric coefficient in Eq. (6.11) and the diamagnetic susceptibility in Eq. (5.7). The first of these also depends on additional parameters Γ and κ; while the former reflects the pair damping, the latter reflects the particle-hole asymmetry which accompanies long-lived pairs. It is clear from the expressions in Eqs. (5.7) and (6.11) that the simple ratio of $2\hbar/c$ between the absolute magnetization and transverse thermoelectric coefficient, in the linear magnetic field regime, is only expected to be correct in the weak-fluctuation limit. As pairing becomes stronger, the transverse thermoelectric response becomes progressively larger than its diamagnetic counterpart. This is because the pairs become longer lived so that Γ becomes much smaller than κ.

The diamagnetic susceptibility and transverse thermoelectric coefficient are dependent on two key parameters: the pair mass $M_{\rm pair}$ and the pair chemical potential $\mu_{\rm pair}$. In the cuprates we find both parameters vary with hole-doping concentration, x. They also both reflect, in slightly different ways, the two important temperatures T^* (pairing onset temperature) and T_c (phase transition temperature). In the simplest terms, $M_{\rm pair}(T,x)$ is more directly reflective of $T_c(x)$ since we find the phase transition temperature vanishes when $M_{\rm pair}$ diverges. By contrast $\mu_{\rm pair}(T,x)$ is more directly reflective of $T^*(x)$ since (as we have shown) a higher pairing onset temperature leads to a stabilization of the pairs and to a reduction in their chemical potential. In this way, both temperature scales play an important role in establishing the behavior of the diamagnetic susceptibility and Nernst coefficient in the high-temperature superconductors.

Note added. Recently, we became aware of Ref. [59] which interprets the onset temperature differently from Refs. [7,14]. However, since the experimental results are in rough agreement with one another, the comparison to our theoretical onset temperatures, as would be obtained following the alternative procedure [59], is expected to again be reasonable.

ACKNOWLEDGMENTS

This work was supported by NSF-DMR-MRSEC 1420709, NSF of China (Grant No. 11274267), and NSF of Zhejiang Province of China (Grant No. LZ13A040001). It is our pleasure to thank Alexey Galda for fruitful discussions and correspondence on this topic.

APPENDIX A: PAIR-PROPAGATOR DERIVATION

This section provides a brief derivation of the GG_0-fluctuation-theory pair propagator introduced in Eq. (2.4). The approach closely follows that of Kadanoff and Martin [33]; for further details see Ref. [27] or Ref. [34]. The four-vector notation $1 \equiv (\mathbf{r}_1,t_1)$, etc., is used throughout. The starting point is the equation of motion for the full single-particle Green's function:

$$G(1-1') = \widetilde{G}_0(1-1') - i\int d\bar{1}\, d\bar{2}\, \widetilde{G}_0(1-\bar{1}) \times V(\bar{1}-\bar{2})L_2(\bar{1}\,\bar{2};1'\bar{2}^+), \tag{A1}$$

where V is the four-body interaction term and $\widetilde{G}_0$ is the single-particle Green's function with the Hartree term included. Here the two-particle correlation function, L_2, is related to the two-particle Green's function, G_2, by

$$L_2(1\,2;1'\,2') = G_2(1\,2;1'\,2') - G(1-1')G(2-2'). \tag{A2}$$

Note that L_2 and G_2 correspond to L^{+-} and G^{+-} in the notation of Ref. [33]. The equation of motion for G_2 can also be constructed, and it will in turn depend on the three-particle Green's function G_3. Continuing in this manner leads to an infinite system of equations for all n-particle Green's functions. To make progress, the system of equations is truncated in such a way that G_3 is expressed solely in terms of G and G_2. This means only two equations of motion, one for G and one for G_2, are needed to determine the form of G. The particular approach for decoupling G_3 in terms of G and G_2 is known as the *pairing approximation* [33]. The approximate equation of motion for G_2, with only the ladder diagrams retained, is then

$$L_2(1\,2;1'\,2') \approx i\int d\bar{1}\, d\bar{2}\, \widetilde{G}_0(1-\bar{1})V(\bar{1}-\bar{2})G(\bar{2}-2)G_2(\bar{1}\,\bar{2};1'\,2'). \tag{A3}$$

The Feynman diagrams for this expression are shown in Fig. 7.

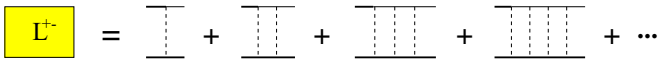

FIG. 7. Diagrams for the two-point correlation function L_2 ($L^{\pm}$ in the notation of Ref. [33]). The solid (thin) line is the full (bare) Green's function, where the "bare" Green's function $\widetilde{G}_0$ includes the Hartree self-energy. The dashed line is the interaction V. This figure is taken from Ref. [34].

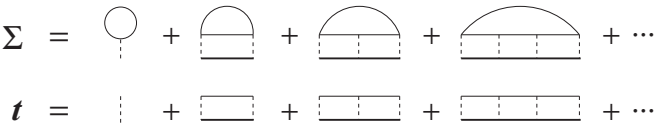

FIG. 8. Diagrams for the self-energy (Σ) and t matrix (t) of the GG_0 pair-fluctuation theory. The external legs have been removed in both diagrams. The solid (thin) line is the full (bare) Green's function, where the "bare" Green's function $\widetilde{G}_0$ includes the Hartree self-energy. The dashed line is the interaction vertex V. This figure is taken from Ref. [34].

These equations are equivalent to Eqs. (2.6)–(2.8) in Ref. [33], which then makes a further assumption in Eq. (2.29) of their paper. Kadanoff and Martin used the above equations to provide a systematic formulation of BCS theory. The asymmetric form in which the Green's functions G and G_0 enter Eqs. (A1) and (A3) is a consequence of the equations of motion and the pairing approximation [33]; this structure is necessary in order to reproduce the BCS limit. The correlation function L_2 can be easily determined in the weak-coupling (or BCS) limit. In the corresponding superconducting state, L_2 can be factorized into the standard Gorkov Green's functions; see Eq. (2.35) of Ref. [33].

To generalize the above formulation of BCS (weak-pairing) theory and allow for arbitrary coupling strengths, we self-consistently solve Eqs. (A1)–(A3) for both G and L_2. This procedure naturally leads to a nonvanishing L_2 in the normal state, and is suitable for describing *noncondensed* pairing fluctuations. For convenience we convert to momentum space and ignore the explicit arguments in the Green's functions. Define the pair susceptibility, Π, by

$$\Pi = -i\widetilde{G}_0 V G. \tag{A4}$$

Using this definition in Eqs. (A2) and (A3), it follows that

$$L_2 = i\frac{\widetilde{G}_0 V G G G}{1+\Pi}. \tag{A5}$$

In this expression note that $\widetilde{G}_0$ and G are external legs, hence the reason why Π is not written in the numerator. An additional approximation is now made; the GG pair in the numerator is replaced by $\widetilde{G}_0 G$. Since the superconducting instability is determined by the pole in the two-particle Green's function L_2, this represents a rather benign assumption. Inserting the resulting expression for L_2 into Eq. (A1), we obtain

$$G = \widetilde{G}_0 + i\widetilde{G}_0 V\frac{\Pi}{1+\Pi}\widetilde{G}_0 G. \tag{A6}$$

The self-energy, $\Sigma = \widetilde{G}_0^{-1} - G^{-1}$, is thus

$$\Sigma = i\frac{V\Pi}{1+\Pi}\widetilde{G}_0. \tag{A7}$$

To simplify the above expression, instead of including the Hartree self-energy in a modified "bare" Green's function $\widetilde{G}_0$, we add the lowest order Hartree self-energy term, $-iVG_0$, to Eq. (A7) and everywhere replace $\widetilde{G}_0$ by G_0. Since the Hartree self-energy corresponds to a small change in chemical potential, this assumption does not modify the central physics. With this assumption the self-energy now becomes

$$\Sigma = \frac{-iVG_0}{1+\Pi} \equiv tG_0, \quad t = \frac{-iV}{1+\Pi}. \tag{A8}$$

In the imaginary-time formalism the above equation becomes

$$\Sigma = tG_0, \quad t = \frac{V}{1+\Pi}, \quad \Pi = VG_0G. \tag{A9}$$

For a separable potential, $V(k,k') = g\varphi_{\mathbf{k}}\varphi_{\mathbf{k}'}$, g can be factored out of Π to give

$$\Pi(q) = \sum_k G(k)G_0(-k+q)\varphi^2_{\mathbf{k}-\mathbf{q}/2}. \tag{A10}$$

Here q is the total momentum, while k and $-k+q$ are the momenta of each propagator in the particle-particle ladder. Similarly, the t matrix now becomes $t(k,k';q) = t(q)\varphi_{\mathbf{k}}\varphi_{\mathbf{k}'}$. This allows $t(q)$, which depends only on the bosonic momentum q, to be used as the new definition of the t matrix. As a result, the self-energy is

$$\Sigma(k) = \sum_q t(q)G_0(-k+q)\varphi^2_{\mathbf{k}-\mathbf{q}/2}, \tag{A11}$$

and the t matrix is

$$t(q) = \frac{g}{1+g\Pi(q)}. \tag{A12}$$

With Π determined in Eq. (A10), this now reproduces the definition of the t matrix given in Eq. (2.4). The Feynman diagrams for the self-energy and t matrix are shown in Fig. 8.

APPENDIX B: OBTAINING THE FULL EM VERTEX USING THE WARD-TAKAHASHI IDENTITY

1. GG_0 pair-fluctuation theory

In this section the Ward-Takahashi identity (WTI) is used to derive the full electromagnetic (EM) vertex for the GG_0 pair-fluctuation theory, which appears in Eqs. (4.3)–(4.6) of the main text. The WTI for the full EM vertex is [38]

$$\begin{aligned} q_\mu\Gamma^\mu_{\rm E}(k_+,k_-) &= G^{-1}(k_+) - G^{-1}(k_-) \\ &= q_\mu\gamma^\mu_{\rm E}(k_+,k_-) + \Sigma(k_-) - \Sigma(k_+). \end{aligned} \tag{B1}$$

Here $k_\pm \equiv k \pm q/2$. The self-energy for the GG_0 pair-fluctuation theory is $\Sigma(k) = \sum_p t(p)G_0(p-k) = \sum_p t(p+k)G_0(p)$, where the t matrix is defined through the pair susceptibility by $t^{-1}(p) = g^{-1} + \Pi(p)$, with $\Pi(p) = \sum_l G_0(p-l)G(l) = \sum_l G(p-l)G_0(l)$ the definition of the pair susceptibility. Throughout this paper k,l denote fermionic four-momenta: $k^\mu = (i\omega_n,\mathbf{k})$, $l^\mu = (i\epsilon_n,\mathbf{l})$, where ω_n and ϵ_n are fermionic Matsubara frequencies, whereas p,q denote bosonic four-momenta: $p^\mu = (i\varpi_m,\mathbf{p})$, $q^\mu = (i\Omega_m,\mathbf{q})$, where ϖ_m and

Ω_m are bosonic Matsubara frequencies. Using the two equivalent forms of the self-energy given above, the self-energy difference appearing in Eq. (B1) becomes

$$\Sigma(k_-) - \Sigma(k_+) = \sum_p t(p)G_0(p-k_-)\big[G_0^{-1}(p-k_-) - G_0^{-1}(p-k_+)\big]G_0(p-k_+) + 2\sum_p G_0(p)t(p+k_+)[t^{-1}(p+k_+) - t^{-1}(p+k_-)]t(p+k_-). \tag{B2}$$

By using the bare WTI, the term in square brackets on the first line is given by the contraction $q_\mu\gamma_{\rm E}^\mu(p-k_-,p-k_+)$. From the definition of the t matrix, the difference of the two inverse t matrices is

$$t^{-1}(p+k_+) - t^{-1}(p+k_-) = \Pi(p+k_+) - \Pi(p+k_-). \tag{B3}$$

Using the two equivalent forms of the pair susceptibility, the pair susceptibility difference becomes

$$2[\Pi(p+k_+) - \Pi(p+k_-)] = -\sum_l G_0(l)G(p+k_+-l)[G^{-1}(p+k_+-l) - G^{-1}(p+k_--l)]G(p+k_--l) - \sum_l G(l)G_0(p+k_+-l)\big[G_0^{-1}(p+k_+-l) - G_0^{-1}(p+k_--l)\big]G_0(p+k_--l). \tag{B4}$$

From the WTI, the first term in square brackets is the contraction $q_\mu\Gamma_{\rm E}^\mu(p+k_+-l,p+k_--l)$; similarly the second term in square brackets is the contraction $q_\mu\gamma_{\rm E}^\mu(p+k_+-l,p+k_--l)$. Inserting these results into Eqs. (B2) and (B3) then gives

$$\begin{aligned}\Sigma(k_-) - \Sigma(k_+) = {}& \sum_p t(p)G_0(p-k_-)q_\mu\gamma_{\rm E}^\mu(p-k_-,p-k_+)G_0(p-k_+)\\ & - \sum_p G_0(p)t(p+k_+)\sum_l G_0(l)G(p+k_+-l)q_\mu\Gamma_{\rm E}^\mu(p+k_+-l,p+k_--l)G(p+k_--l)t(p+k_-)\\ & - \sum_p G(p)t(p+k_+)\sum_l G(l)G_0(p+k_+-l)q_\mu\gamma_{\rm E}^\mu(p+k_+-l,p+k_--l)G_0(p+k_--l)t(p+k_-).\end{aligned} \tag{B5}$$

In the second and third lines, first let $p \to p-k$, and then after that let $l \to p-l$. Inserting the resulting expression into Eq. (B1), and solving for the full EM vertex, then gives the following result:

$$\begin{aligned}\Gamma_{\rm E}^\mu(k_+,k_-) = {}& \gamma_{\rm E}^\mu(k_+,k_-) + \sum_p t(p)G_0(p-k_-)\gamma_{\rm E}^\mu(p-k_-,p-k_+)G_0(p-k_+)\\ & - \sum_p\sum_l t(p_-)t(p_+)G_0(p-k)G_0(p-l)G(l_+)\Gamma_{\rm E}^\mu(l_+,l_-)G(l_-)\\ & - \sum_p\sum_l t(p_-)t(p_+)G_0(p-k)G(p-l)G_0(l_+)\gamma_{\rm E}^\mu(l_+,l_-)G_0(l_-).\end{aligned} \tag{B6}$$

This reproduces the full EM vertex given in Eqs. (4.3)–(4.6) of the main text. The first term in the first line is the bare EM vertex $\gamma_{\rm E}^\mu$, the second term in the first line is the Maki-Thompson vertex $\mathrm{MT}_{\rm E}^\mu$, the second line is the Aslamazov-Larkin vertex $\mathrm{AL}_{\rm E,1}^\mu$, and the third line is the other Aslamazov-Larkin vertex $\mathrm{AL}_{\rm E,2}^\mu$. The Feynman diagrams for the full EM vertex are given in Fig. 9.

An important identity mentioned in Sec. IV of the main text, which relates the Maki-Thompson vertex to the Aslamazov-Larkin vertices, is $q_\mu[2\mathrm{MT}_{\rm E}^\mu(k^+,k^-) + \mathrm{AL}_{\rm E,1}^\mu(k^+,k^-) + \mathrm{AL}_{\rm E,2}^\mu(k^+,k^-)] = 0$. This is proved directly as follows. By applying the bare WTI to the MT vertex in Eq. (B6), it follows that

$$q_\mu\mathrm{MT}_{\rm E}^\mu(k^+,k^-) = \sum_p t(p)[G_0(p-k_+) - G_0(p-k_-)] = \Sigma(k_+) - \Sigma(k_-). \tag{B7}$$

Similarly, by applying the bare and full WTIs to the AL vertices in Eq. (B6), it follows that

$$\begin{aligned}q_\mu\big[\mathrm{AL}_{\rm E,1}^\mu(k_+,k_-) + \mathrm{AL}_{\rm E,2}^\mu(k_+,k_-)\big] = {}& -\sum_p t(p_-)t(p_+)G_0(p-k)\sum_l G_0(p-l)[G(l_-) - G(l_+)]\\ & - \sum_p t(p_-)t(p_+)G_0(p-k)\sum_l G(p-l)[G_0(l_-) - G_0(l_+)]\\ = {}& -2\sum_p t(p_-)t(p_+)G_0(p-k)[\Pi(p_-) - \Pi(p_+)]\end{aligned}$$

$$= -2\sum_p [t(p_+) - t(p_-)]G_0(p-k)$$

$$= -2[\Sigma(k_+) - \Sigma(k_-)]. \tag{B8}$$

From Eqs. (B7) and (B8) the desired result follows: $q_\mu[2\mathrm{MT}^\mu_{\mathrm{E}}(k^+,k^-) + \mathrm{AL}^\mu_{\mathrm{E},1}(k^+,k^-) + \mathrm{AL}^\mu_{\mathrm{E},2}(k^+,k^-)] = 0$.

Once the full EM vertex has been determined, the exact EM response functions can be computed via

$$P^{\mu\nu}(q) = 2\sum_k G(k_+)\Gamma^\mu_{\mathrm{E}}(k_+,k_-)G(k_-)\gamma^\nu_{\mathrm{E}}(k_-,k_+). \tag{B9}$$

The Feynman diagrams for the exact EM response functions are given in Fig. 10. Since the full EM vertex itself appears in the first Aslamazov-Larkin diagram ($\mathrm{AL}_{\mathrm{E},1}$), the explicit closed form of the full EM vertex for the GG_0 pair-fluctuation theory cannot be obtained. The result is a complicated integral equation that is theoretically intractable.

2. G_0G_0 pair-fluctuation theory

The previous section derived the full EM response for the GG_0 pair-fluctuation theory. A similar derivation can be performed for the G_0G_0 pair-fluctuation theory. Since the calculation is almost identical to the one performed in the previous section, only the final results are given. The self-energy for the G_0G_0 pair-fluctuation theory is $\Sigma(k) = \sum_p t(p)G_0(p-k) = \sum_p t(p+k)G_0(p)$, where the t matrix is defined through the pair susceptibility by $t^{-1}(p) = g^{-1} + \Pi(p)$, with $\Pi(p) = \sum_l G_0(p-l)G_0(l)$ the pair susceptibility. The pair susceptibility in this theory has two identical bare Green's functions. This means that when all possible vertex insertions in the self-energy are performed, two identical Aslamazov-Larkin diagrams will arise from the two bare vertex insertions in the Green's functions in the pair susceptibility. Following the same procedure as in the previous section, the full EM vertex is given by

$$\Gamma^\mu_{\mathrm{E}}(k_+,k_-) = \gamma^\mu_{\mathrm{E}}(k_+,k_-) + \sum_p t(p)G_0(p-k_-)\gamma^\mu_{\mathrm{E}}(p-k_-,p-k_+)G_0(p-k_+)$$

$$- 2\sum_p\sum_l t(p_-)t(p_+)G_0(p-k)G_0(p-l)G_0(l_+)\gamma^\mu_{\mathrm{E}}(l_+,l_-)G_0(l_-). \tag{B10}$$

The Feynman diagrams for the exact EM response functions are given in Fig. 11. Notice that, in contrast to the GG_0 pair-fluctuation theory, the full EM vertex itself does not appear in either the Maki-Thompson or Aslamazov-Larkin diagrams. Therefore, provided the t matrix is known exactly, in principle the explicit closed form of the full EM vertex for the G_0G_0 pair-fluctuation theory can be obtained.

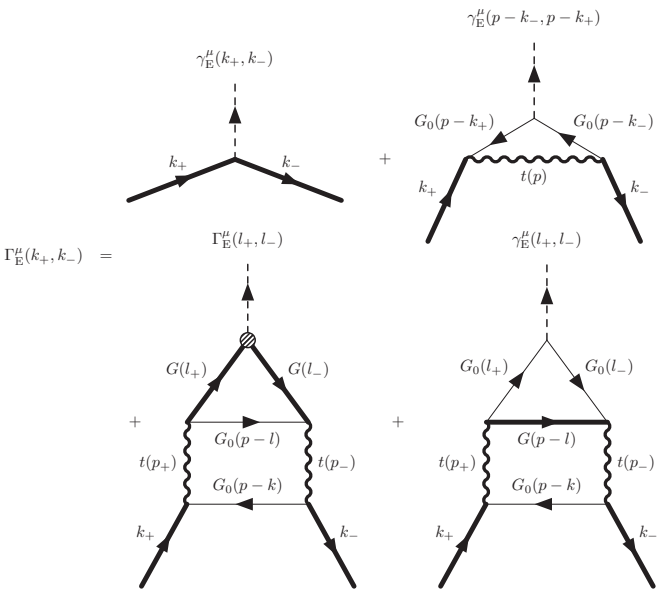

FIG. 9. Feynman diagrams for the full EM vertex in the GG_0 pair-fluctuation theory.

Note the distinction between Figs. 10 and 11; the GG_0 pair-fluctuation theory contains dressed t matrices, and the Aslamazov-Larkin diagrams $\mathrm{AL}_{\mathrm{E},1}$ and $\mathrm{AL}_{\mathrm{E},2}$ have two and one dressed Green's functions, respectively, appearing in the leftmost triangle vertex. In contrast the G_0G_0 pair-fluctuation theory has t matrices constructed solely of bare Green's functions, and two identical Aslamazov-Larkin diagrams with only bare Green's functions and bare vertices in the leftmost triangle vertex.

The standard response functions considered in the weak-fluctuation literature arise by expanding the diagrams in Fig. 11 to lowest order, that is, by expanding the Green's functions according to a truncated Dyson's equation: $G \approx G_0 + G_0\Sigma G_0$. Performing this expansion on the diagrams in Fig. 11, the result is the normal state "bubble," two density of states, one Maki-Thompson, and two identical Aslamazov-Larkin diagrams, all with bare Green's functions and bare vertices. This reproduces the Feynman diagrams in Ref. [20]. However, it is not a gauge-invariant set of diagrams, and only satisfies the WTI to $O(\Sigma)$ [42]. These diagrams are shown in Fig. 12.

APPENDIX C: DIAMAGNETIC SUSCEPTIBILITY IN THE SMALL-$|\mu_{\mathrm{pair}}|$ LIMIT

In Sec. V of the main text, the contribution to diamagnetic susceptibility from the Aslamazov-Larkin diagrams was

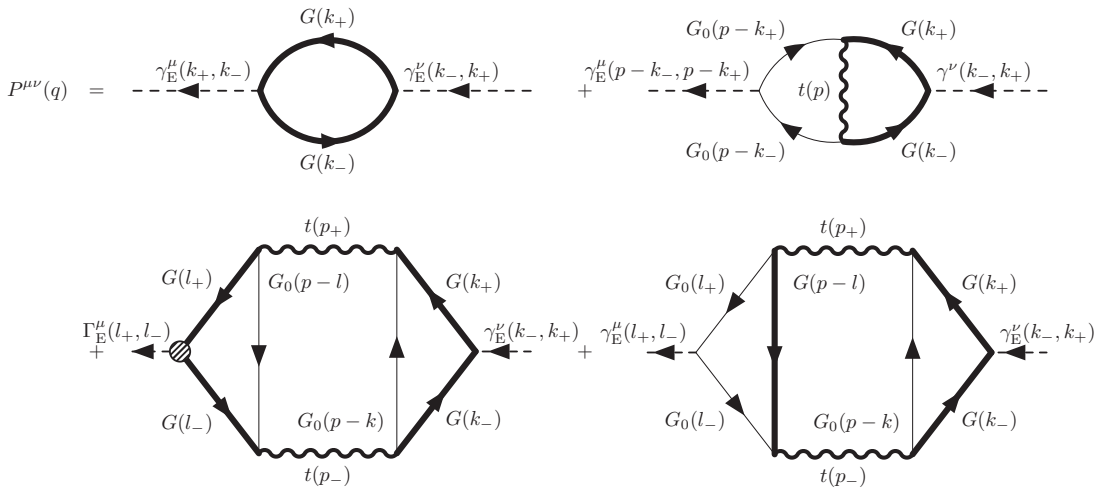

FIG. 10. Feynman diagrams for the exact EM response functions in the GG_0 pair-fluctuation theory. In order from left to right, and top to bottom, there is one "bubble," one Maki-Thompson, one Aslamazov-Larkin ($\mathrm{AL_{E,1}}$), and another (nonidentical) Aslamazov-Larkin ($\mathrm{AL_{E,2}}$) diagram.

obtained in the small-$|\mu_{\rm pair}|$ limit. The calculation was simplified by ignoring the Matsubara frequency summation and just treating the integrand with zero bosonic Matsubara frequency. This is justified in the small-$|\mu_{\rm pair}|$ limit, and was also performed in the seminal paper [20] of Aslamazov and Larkin. In this appendix the Matsubara frequency summation is performed, and a complete calculation of diamagnetic susceptibility in the small-$|\mu_{\rm pair}|$ limit is presented. The starting point is Eq. (5.4) of the main text:

$$\chi_{\rm dia} = e^2 \sum_p \left[\frac{\partial \Pi(p)}{\partial p^x}\right]^2 \left\{ t(p) \frac{\partial^2 t(p)}{\partial (p^y)^2} - \left[\frac{\partial t(p)}{\partial p^y}\right]^2 \right\}. \quad \text{(C1)}$$

The t matrix is related to the pair susceptibility by $t^{-1}(p) = g^{-1} + \Pi(p)$; thus it follows that $\partial t(p)/\partial p^y = -t^2(p)[\partial t^{-1}(p)/\partial p^y] = -t^2(p)[\partial \Pi(p)/\partial p^y]$. Similarly $\partial^2 t(p)/\partial (p^y)^2 = 2t^3(p)[\partial \Pi(p)/\partial p^y]^2 - t^2(p)[\partial^2 \Pi(p)/\partial (p^y)^2]$. Therefore, using these identities gives

$$\chi_{\rm dia} = e^2 \sum_p \left[\frac{\partial \Pi(p)}{\partial p^x}\right]^2 \left\{ t^4(p) \left[\frac{\partial \Pi(p)}{\partial p^y}\right]^2 - t^3(p) \frac{\partial^2 \Pi(p)}{\partial (p^y)^2} \right\}. \quad \text{(C2)}$$

The term that is quartic in the t matrix can be simplified as follows:

$$\sum_p \left[\frac{\partial \Pi(p)}{\partial p^x}\right]^2 t^4(p) \left[\frac{\partial \Pi(p)}{\partial p^y}\right]^2 = -\sum_p \left[\frac{\partial \Pi(p)}{\partial p^x}\right]^2 \frac{\partial \Pi(p)}{\partial p^y} \frac{\partial t(p)}{\partial p^y} t^2(p)$$

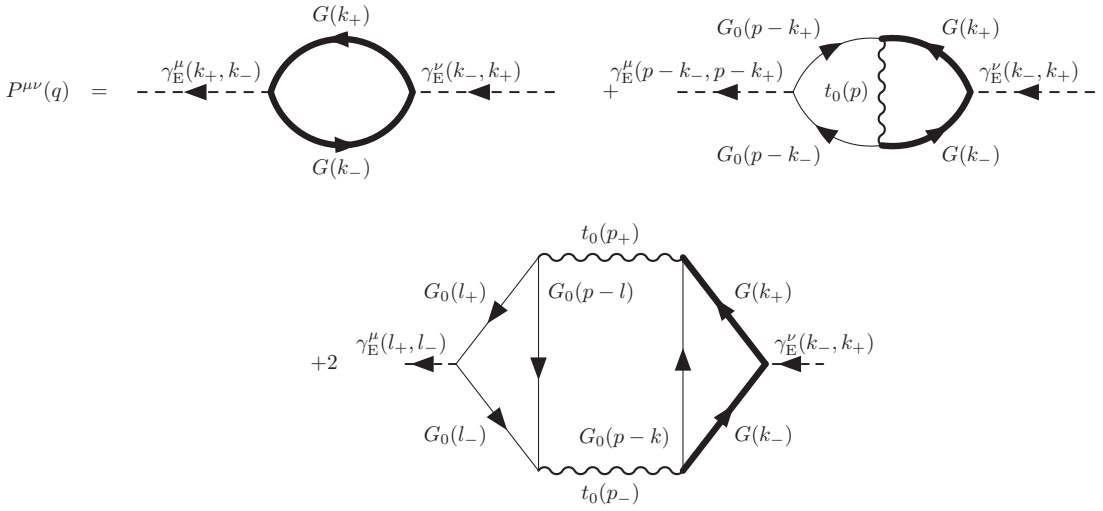

FIG. 11. Feynman diagrams for the exact EM response functions in the G_0G_0 pair-fluctuation theory. In order from left to right, and top to bottom, there is one "bubble," one Maki-Thompson, and two identical Aslamazov-Larkin diagrams.

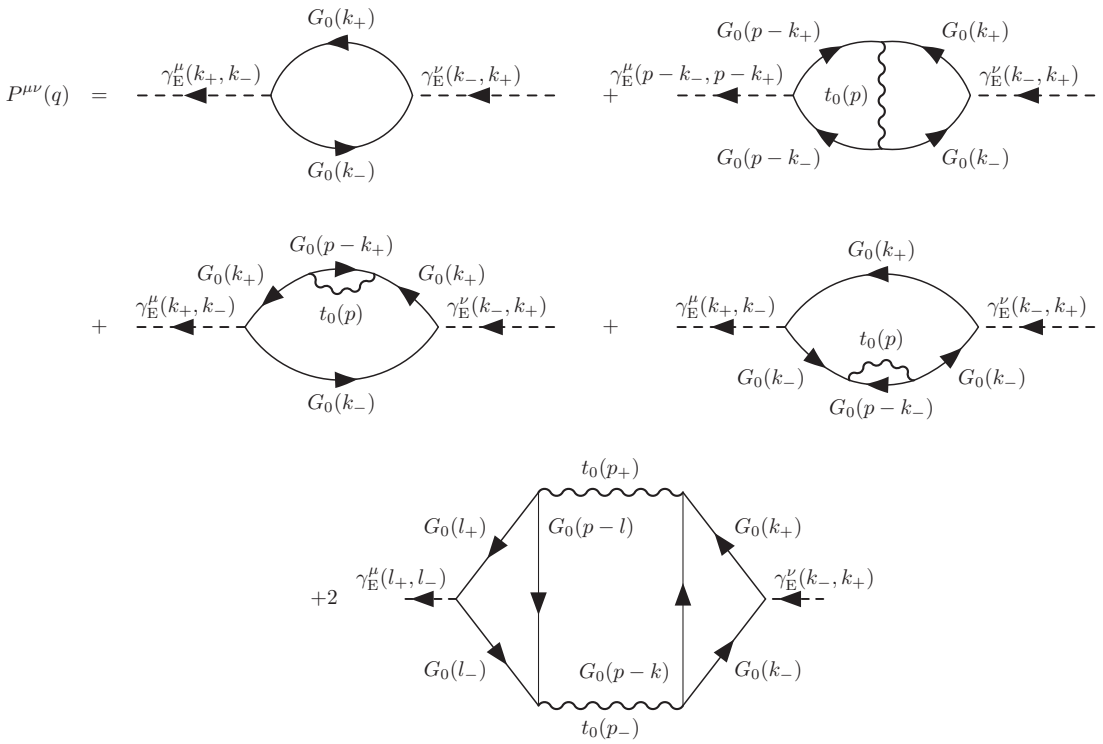

FIG. 12. Lowest order Feynman diagrams for the EM response functions in the G_0G_0 pair-fluctuation theory. In order from left to right, and top to bottom, there is a normal state "bubble," one Maki-Thompson, two density of states, and two identical Aslamazov-Larkin diagrams.

$$= -\frac{1}{3}\sum_p \left[\frac{\partial\Pi(p)}{\partial p^x}\right]^2 \frac{\partial\Pi(p)}{\partial p^y}\frac{\partial t^3(p)}{\partial p^y}$$

$$= \frac{1}{3}\sum_p t^3(p)\left\{\left[\frac{\partial\Pi(p)}{\partial p^x}\right]^2 \frac{\partial^2\Pi(p)}{\partial (p^y)^2} + 2\frac{\partial\Pi(p)}{\partial p^y}\frac{\partial\Pi(p)}{\partial p^x}\frac{\partial^2\Pi(p)}{\partial p^y \partial p^x}\right\}. \quad \text{(C3)}$$

Inserting this result into Eq. (C2) and then simplifying gives the diamagnetic susceptibility as

$$\chi_{\rm dia} = -\frac{2e^2}{3}\sum_p t^3(p)\left\{\left[\frac{\partial\Pi(p)}{\partial p^x}\right]^2 \frac{\partial^2\Pi(p)}{\partial (p^y)^2} - \frac{\partial\Pi(p)}{\partial p^y}\frac{\partial\Pi(p)}{\partial p^x}\frac{\partial^2\Pi(p)}{\partial p^y \partial p^x}\right\}. \quad \text{(C4)}$$

This is a general expression for the diamagnetic susceptibility due to the dominant contribution in the Aslamazov-Larkin diagrams. Note that for the case of the weak-fluctuation theory, where the pair susceptibility is $\Pi(p) = \sum_l G_0(p-l)G_0(l)$, Eq. (C4) is equivalent to Eq. (17) of the Aslamazov-Larkin paper [20].

To obtain the diamagnetic susceptibility in the small-$|\mu_{\rm pair}|$ limit, we now use the small-momentum form of the pair propagator, as defined in Eq. (1.1) of the main text: $t_{\rm R}^{-1}(\varpi,\mathbf{p}) = Z[\kappa\varpi - \mathbf{p}^2/(2M_{\rm pair}) - |\mu_{\rm pair}| + i\Gamma\varpi]$, and the definition $t^{-1}(p) = g^{-1} + \Pi(p)$. Evaluating the spatial derivatives in Eq. (C4) gives $\partial\Pi(p)/\partial p^x = \partial t^{-1}(p)/\partial p^x = -Zp^x/M_{\rm pair}$, $\partial^2\Pi(p)/\partial(p^y)^2 = -Z/M_{\rm pair}$, and $\partial^2\Pi(p)/\partial p^x\partial p^y = 0$. Inserting these results into Eq. (C4) then gives the first line of Eq. (5.6) of the main text, where the Matsubara frequency summation has been restored:

$$\chi_{\rm dia} = \frac{2e^2}{3M_{\rm pair}}\sum_p \left(\frac{p^x}{M_{\rm pair}}\right)^2 [Zt(p)]^3. \quad \text{(C5)}$$

To simplify this expression, note that $\partial t^{-1}(p)/\partial p^x = -Zp^x/M_{\rm pair}$ and $\partial t(p)/\partial p^x = -t^2(p)[\partial t^{-1}(p)/\partial p^x] = Zt^2(p)p^x/M_{\rm pair}$. Using these identities, along with performing integration by parts, the diamagnetic susceptibility becomes

$$\chi_{\rm dia} = \frac{2e^2}{3M_{\rm pair}}\sum_p \frac{Z^2p^x}{M_{\rm pair}}t(p)\frac{\partial t(p)}{\partial p^x} = \frac{e^2}{3M_{\rm pair}}\sum_p \frac{Z^2p^x}{M_{\rm pair}}\frac{\partial t^2(p)}{\partial p^x} = -\frac{e^2}{3M_{\rm pair}^2}\sum_p [Zt(p)]^2. \quad \text{(C6)}$$

To perform the Matsubara frequency summation, we use the Eliashberg contour [5] and the identity (valid for bosonic Matsubara frequencies) [5,32]

$$T\sum_{i\varpi_m} f(i\varpi_m) = \frac{1}{4\pi i}\oint_{\mathcal{C}} dz\, \coth\left(\frac{1}{2}\beta z\right) f(z), \quad \text{(C7)}$$

where $\beta = 1/(k_BT)$ and we set $k_B = 1$. Here $\mathcal{C}$ is a closed contour enclosing the poles of $\coth(\beta z/2)$, which occur at the bosonic Matsubara frequencies $z = i\varpi_m = 2\pi imT$, where $m \in \mathbb{Z}$. Since the semicircle contribution to the integral in Eq. (C6) vanishes, the contour integral can be deformed to an

integral above and below the real axis. Thus the diamagnetic susceptibility becomes

$$\chi_{\rm dia} = -\frac{Z^2e^2}{3M_{\rm pair}^2}\sum_{\mathbf{p}}\frac{1}{4\pi i}\int_{-\infty}^{\infty}dx\,\coth\left(\frac{1}{2}\beta x\right)\left[t_{\rm R}^2(x,\mathbf{p})-t_{\rm A}^2(x,\mathbf{p})\right]$$
$$= -\frac{Z^2e^2}{3\pi M_{\rm pair}^2}\sum_{\mathbf{p}}\int_{-\infty}^{\infty}dx\,\coth\left(\frac{1}{2}\beta x\right){\rm Re}[t_{\rm R}(x,\mathbf{p})]{\rm Im}[t_{\rm R}(x,\mathbf{p})]. \tag{C8}$$

Here $t_{\rm R}$ and $t_{\rm A}$ denote the retarded and advanced propagators, which are related by $t_{\rm A}(z,\mathbf{p}) = t_{\rm R}(z,\mathbf{p})^*$.

In the small-$|\mu_{\rm pair}|$ limit the main contribution to the integral occurs when $\beta x \ll 1$, which allows the coth function to be expanded as $\coth(\beta x/2) \approx 2T/x$. Inserting the retarded propagator, defined by $t_{\rm R}^{-1}(x,\mathbf{p}) = Z[\kappa x - \mathbf{p}^2/(2M_{\rm pair}) - |\mu_{\rm pair}| + i\Gamma x]$, into the above expression then gives

$$\chi_{\rm dia} = \frac{2e^2T\Gamma}{3\pi M_{\rm pair}^2}\sum_{\mathbf{p}}\int_{-\infty}^{\infty}dx\,\frac{\kappa x - \mathbf{p}^2/(2M_{\rm pair}) - |\mu_{\rm pair}|}{[(\kappa x - \mathbf{p}^2/(2M_{\rm pair}) - |\mu_{\rm pair}|)^2 + (\Gamma x)^2]^2}$$
$$= -\frac{4e^2T}{3}\sum_{\mathbf{p}}\frac{1}{(\mathbf{p}^2 + 2M_{\rm pair}|\mu_{\rm pair}|)^2}$$
$$= -\frac{e^2T}{3\pi^2}\int_{-\infty}^{\infty}dp\,\frac{p^2}{(p^2 + 2M_{\rm pair}|\mu_{\rm pair}|)^2}. \tag{C9}$$

The remaining p integration is easily performed using a closed contour integral in the upper half plane and evaluating the residue at the pole $p = i(2M_{\rm pair}|\mu_{\rm pair}|)^{1/2}$. This gives, after restoring the constants $\hbar$, k_B, and c,

$$\chi_{\rm dia} = -\frac{k_BT(2e)^2}{24\pi\hbar c^2}\sqrt{\frac{1/(2M_{\rm pair})}{|\mu_{\rm pair}|}}. \tag{C10}$$

The diamagnetic susceptibility is written in this form to compare with the free boson result, which is derived in the next section. The above expression reproduces Eq. (5.7) of the main text, and validates the approximation made there concerning setting the bosonic Matsubara frequency to zero in the integrand.

APPENDIX D: FREE BOSON DIAMAGNETIC SUSCEPTIBILITY

This section derives the diamagnetic susceptibility for free bosons and also gives the limiting form when the chemical potential tends to zero. While the free boson diamagnetic susceptibility is well known, the aim here is to express it in an identical form to the Aslamazov-Larkin contribution to diamagnetic susceptibility for the GG_0 pair-fluctuation theory.

The Kubo formula for diamagnetic susceptibility, $\chi_{\rm dia}$, is given in Eq. (3.3) of the main text:

$$\chi_{\rm dia} = -\lim_{\mathbf{q}\to 0}\left[\frac{P^{xx}(i\Omega_m = 0,\mathbf{q}) + n/m}{\mathbf{q}^2}\right]_{q^x=q^z=0}. \tag{D1}$$

Recall that $P^{xx}(0) = -n/m$ above T_c. The response function for spin-0 free bosons is given by

$$P^{xx}(q) = -(e^*)^2\sum_p G_0(p_+)\gamma_{\rm E}^x(p_+,p_-)G_0(p_-)\gamma_{\rm E}^x(p_-,p_+), \tag{D2}$$

where the bare Green's function is $G_0^{-1}(p) = i\varpi_m - \xi_{\mathbf{p}}$, with $\xi_{\mathbf{p}} = \mathbf{p}^2/(2m_{\rm b}) - \mu_{\rm b}$ the free particle dispersion, and the bare vertex is $\gamma_{\rm E}^x(p_+,p_-) = p^x/m_{\rm b}$. Here $m_{\rm b}$ and $\mu_{\rm b}$ are the free boson mass and chemical potential, respectively. The four-vectors p^μ, q^μ are $p^\mu = (i\varpi_m,\mathbf{p})$, $q^\mu = (i\Omega_m,\mathbf{q})$, where ϖ_m, Ω_m are both bosonic Matsubara frequencies, and $p_\pm \equiv p \pm q/2$. The four-vector summation is defined by $\sum_p = T\sum_{i\varpi_m}\sum_{\mathbf{p}}$, where T is the temperature. Note the relative sign difference compared to the fermionic response function in Eq. (3.1) of the main text.

Expanding out the Green's functions in Eq. (D2) to $O(\mathbf{q}^2)$ and then using Eq. (D1), the free boson diamagnetic susceptibility becomes

$$\chi_{\rm b} = \frac{(e^*)^2}{4}\sum_p\left\{G_0(p)\frac{\partial^2G_0(p)}{\partial(p^y)^2} - \left[\frac{\partial G_0(p)}{\partial p^y}\right]^2\right\}\left(\frac{p^x}{m_{\rm b}}\right)^2. \tag{D3}$$

Comparing this expression with that appearing in Eq. (5.4) of the main text proves the claim at the beginning of this section, namely that the Aslamazov-Larkin contribution to diamagnetic susceptibility is of the free boson form but with modified vertices and propagators. Now perform integration by parts on the first term to obtain

$$\chi_{\rm b} = -\frac{(e^*)^2}{2}\sum_p\left[\frac{\partial G_0(p)}{\partial p^y}\right]^2\left(\frac{p^x}{m_{\rm b}}\right)^2. \tag{D4}$$

Another expression involving the product of four Green's functions, which has occurred in the fermion literature [60], can also be obtained:

$$\chi_{\rm b} = -\frac{(e^*)^2}{2}\sum_p\left[\frac{\partial G_0(p)}{\partial p^y}\right]^2\left(\frac{p^x}{m_{\rm b}}\right)^2$$
$$= -\frac{(e^*)^2}{2}\sum_p\left[G_0^2(p)\frac{\partial G_0^{-1}(p)}{\partial p^y}\right]^2\left(\frac{p^x}{m_{\rm b}}\right)^2$$
$$= -\frac{(e^*)^2}{2}\sum_p G_0^4(p)\left(\frac{p^y}{m_{\rm b}}\right)^2\left(\frac{p^x}{m_{\rm b}}\right)^2. \tag{D5}$$

The analogous formula for spin-$\frac{1}{2}$ fermions agrees with Ref. [60]. Another equivalent expression for the free boson diamagnetic susceptibility can also be obtained, which is identical in form to the Aslamazov-Larkin contribution found in Eq. (5.6) of the main text. By performing integration by parts on the second term in Eq. (D3), the diamagnetic susceptibility can be expressed as follows:

$$\begin{aligned}\chi_{\rm b} &= \frac{(e^*)^2}{2}\sum_p G_0(p)\frac{\partial^2 G_0(p)}{\partial (p^y)^2}\left(\frac{p^x}{m_{\rm b}}\right)^2 \\ &= \frac{(e^*)^2}{2}\sum_p G_0(p)\frac{\partial}{\partial p^y}\left[G_0^2(p)\frac{p^y}{m_{\rm b}}\right]\left(\frac{p^x}{m_{\rm b}}\right)^2 \\ &= \frac{(e^*)^2}{2}\sum_p G_0(p)\left[\frac{1}{m_{\rm b}}G_0^2(p)+2G_0(p)\frac{\partial G_0(p)}{\partial p^y}\frac{p^y}{m_{\rm b}}\right]\left(\frac{p^x}{m_{\rm b}}\right)^2 \\ &= \frac{(e^*)^2}{2}\sum_p G_0(p)\left[\frac{1}{m_{\rm b}}G_0^2(p)-2G_0^3(p)\frac{\partial G_0^{-1}(p)}{\partial p^y}\frac{p^y}{m_{\rm b}}\right]\left(\frac{p^x}{m_{\rm b}}\right)^2 \\ &= \frac{(e^*)^2}{2}\sum_p G_0^3(p)\left[\frac{1}{m_{\rm b}}+2G_0(p)\left(\frac{p^y}{m_{\rm b}}\right)^2\right]\left(\frac{p^x}{m_{\rm b}}\right)^2. \end{aligned} \tag{D6}$$

Equating this expression with Eq. (D5) then gives

$$\chi_{\rm b} = \frac{(e^*)^2}{6m_{\rm b}}\sum_p\left(\frac{p^x}{m_{\rm b}}\right)^2 G_0^3(p). \tag{D7}$$

Comparison of this equation with that appearing in the first line of Eq. (5.6) of the main text shows that the Aslamazov-Larkin contribution to diamagnetic susceptibility is equivalent to the free boson diamagnetic susceptibility with free boson charge $e^* = 2e$, mass $m_{\rm b} = M_{\rm pair}$, and chemical potential $\mu_{\rm b} = \mu_{\rm pair}$. This shows that in the small-$|\mu_{\rm pair}|$ limit, the underlying effect of the fermionic interactions in the GG_0 pair-fluctuation theory is to modify the free boson parameters. Such an effect is intuitive in the deep BEC regime, where the paired degrees of freedom behave as fluctuating bosons.

The expression in Eq. (D7) can be simplified as follows:

$$\begin{aligned}\chi_{\rm b} &= \frac{(e^*)^2}{6m_{\rm b}}\sum_p\left(\frac{p^x}{m_{\rm b}}\right)^2 G_0^3(p) \\ &= \frac{(e^*)^2}{6m_{\rm b}}\sum_p\left(\frac{p^x}{m_{\rm b}}\right)G_0(p)\frac{\partial G_0(p)}{\partial p^x} \\ &= -\frac{(e^*)^2}{12m_{\rm b}^2}\sum_p G_0^2(p). \end{aligned} \tag{D8}$$

After performing the Matsubara frequency summation, and then integrating by parts, the free boson diamagnetic susceptibility becomes

$$\begin{aligned}\chi_{\rm b} &= \frac{(e^*)^2}{12m_{\rm b}^2}\sum_{\mathbf{p}}\frac{\partial b(\xi_{\mathbf{p}})}{\partial \xi_{\mathbf{p}}} \\ &= -\frac{(e^*)^2}{24\pi^2 m_{\rm b}}\int_0^\infty dp\; b(\xi_{\mathbf{p}}). \end{aligned} \tag{D9}$$

Here $b(x) = [\exp(\beta x)-1]^{-1}$ is the Bose-Einstein distribution function. In the limit that $|\mu_{\rm b}|/T \ll 1$, the above expression reduces to

$$\chi_{\rm b} = -\frac{k_B T (e^*)^2}{24\pi\hbar c^2}\sqrt{\frac{1/(2m_{\rm b})}{|\mu_{\rm b}|}}. \tag{D10}$$

The constants $\hbar$, k_B, and c have been restored to render $\chi_{\rm b}$ dimensionless. Comparison of Eqs. (D10) and (5.7) of the main text proves the result stated in the main text, namely that the small-$|\mu_{\rm pair}|$ limit of the Aslamazov-Larkin contribution to diamagnetic susceptibility is equivalent to the free boson diamagnetic susceptibility, but with bosonic charge $e^* = 2e$, mass $m_{\rm b} = M_{\rm pair}$, and chemical potential $\mu_{\rm b} = \mu_{\rm pair}$.

APPENDIX E: THERMOELECTRIC RESPONSE

1. Ward-Takahashi identity for energy conservation

In Sec. VI of the main text the full heat vertex was presented along with a discussion of the WTI for energy conservation. Here we explicitly prove that the full heat vertex satisfies the WTI for energy conservation. The full heat vertex, as given in Eqs. (6.3)–(6.7) of the main text, is

$$\Gamma^\mu_{\rm H}(k_+,k_-) = \gamma^\mu_{\rm H}(k_+,k_-) + {\rm MT}^\mu_{\rm H}(k_+,k_-) + \lambda^\mu_{\rm H}(k_+,k_-) + {\rm AL}^\mu_{{\rm H},1}(k_+,k_-) + {\rm AL}^\mu_{{\rm H},2}(k_+,k_-), \tag{E1}$$

where the Maki-Thompson, Aslamazov-Larkin, and $\lambda^\mu_{\rm H}$ heat vertices are

$${\rm MT}^\mu_{\rm H}(k_+,k_-) = \sum_p t(p)G_0(p-k_-)\gamma^\mu_{\rm H}(p-k_-,p-k_+)G_0(p-k_+), \tag{E2}$$

$$\mathrm{AL}^{\mu}_{\mathrm{H},1}(k_+,k_-) = -\sum_p \sum_l t(p_-)t(p_+)G_0(p-k)G_0(p-l)G(l_+)\Gamma^{\mu}_{\mathrm{H}}(l_+,l_-)G(l_-), \tag{E3}$$

$$\mathrm{AL}^{\mu}_{\mathrm{H},2}(k_+,k_-) = -\sum_p \sum_l t(p_-)t(p_+)G_0(p-k)G(p-l)G_0(l_+)\gamma^{\mu}_{\mathrm{H}}(l_+,l_-)G_0(l_-), \tag{E4}$$

$$\lambda^{\mu}_{\mathrm{H}}(k_+,k_-) = \sum_p g^{-1}\delta^{\mu 0}t(p_-)t(p_+)G_0(p-k). \tag{E5}$$

The WTI for energy conservation is expressed as

$$q_\mu \Gamma^{\mu}_{\mathrm{H}}(k_+,k_-) = \omega_- G^{-1}(k_+) - \omega_+ G^{-1}(k_-). \tag{E6}$$

For convenience, this can be equivalently written as $q_\mu\Gamma^{\mu}_{\mathrm{H}}(k_+,k_-) = (k_-)^0 G^{-1}(k_+) - (k_+)^0 G^{-1}(k_-)$, where k^0 denotes the time component of the four-vector $k^\mu = (\omega,\mathbf{k})$.

The contractions of the vertices in Eqs. (E2)–(E5) are computed as follows. Using the bare WTI for energy conservation, the contraction of the MT vertex is

$$\begin{aligned} q_\mu \mathrm{MT}^{\mu}_{\mathrm{H}}(k_+,k_-) &= \sum_p t(p)G_0(p-k_-)\big[(p-k_+)^0 G_0^{-1}(p-k_-) - (p-k_-)^0 G_0^{-1}(p-k_+)\big]G_0(p-k_+) \\ &= \sum_p t(p)[(p-k_+)^0 G_0(p-k_+) - (p-k_-)^0 G_0(p-k_-)] = \sum_p (p-k)^0 G_0(p-k)[t(p_+) - t(p_-)]. \end{aligned} \tag{E7}$$

The contraction of the AL vertices is

$$\begin{aligned} q_\mu\big[\mathrm{AL}^{\mu}_{\mathrm{H},1}(k_+,k_-) + \mathrm{AL}^{\mu}_{\mathrm{H},2}(k_+,k_-)\big] &= -\sum_p \sum_l t(p_-)t(p_+)G_0(p-k)G_0(p-l)G(l_+)[(l_-)^0 G^{-1}(l_+) - (l_+)^0 G^{-1}(l_-)]G(l_-) \\ &\quad - \sum_p \sum_l t(p_-)t(p_+)G_0(p-k)G(p-l)G_0(l_+)[(l_-)^0 G_0^{-1}(l_+) - (l_+)^0 G_0^{-1}(l_-)]G_0(l_-) \\ &= -\sum_p \sum_l t(p_-)t(p_+)G_0(p-k)G_0(p-l)[(l_-)^0 G(l_-) - (l_+)^0 G(l_+)] \\ &\quad - \sum_p \sum_l t(p_-)t(p_+)G_0(p-k)G(p-l)[(l_-)^0 G_0(l_-) - (l_+)^0 G_0(l_+)]. \end{aligned} \tag{E8}$$

Now consider Eq. (E8). In the first term, on the first line, let $l \to p_+ - l$, and in the second term, on the first line, let $l \to p_- - l$, to obtain

$$\begin{aligned} q_\mu\big[\mathrm{AL}^{\mu}_{\mathrm{H},1}(k_+,k_-) + \mathrm{AL}^{\mu}_{\mathrm{H},2}(k_+,k_-)\big] &= -\sum_p \sum_l t(p_-)t(p_+)G_0(p-k)G_0(l_-)G(p-l)(p_-)^0 \\ &\quad + \sum_p \sum_l t(p_-)t(p_+)G_0(p-k)G_0(l_+)G(p-l)(p_+)^0. \end{aligned} \tag{E9}$$

The sum over l can be computed, using the definition of the pair susceptibility: $\Pi(p_\pm) = \sum_l G_0(l_\pm)G(p-l)$. Performing the l summation, then using the definition $t^{-1}(p) = g^{-1} + \Pi(p)$ and simplifying, it follows that

$$\begin{aligned} &q_\mu\big[\mathrm{AL}^{\mu}_{\mathrm{H},1}(k_+,k_-) + \mathrm{AL}^{\mu}_{\mathrm{H},2}(k_+,k_-)\big] \\ &= -\sum_p t(p_-)t(p_+)G_0(p-k)\Pi(p_-)(p_-)^0 + \sum_p t(p_-)t(p_+)G_0(p-k)\Pi(p_+)(p_+)^0 \\ &= -\sum_p t(p_+)G_0(p-k)(p_-)^0 + \sum_p t(p_-)G_0(p-k)(p_+)^0 - q^0 g^{-1}\sum_p t(p_-)t(p_+)G_0(p-k). \end{aligned} \tag{E10}$$

The contraction of the $\lambda^{\mu}_{\mathrm{H}}$ vertex is easily computed to give

$$q_\mu \lambda^{\mu}_{\mathrm{H}}(k_+,k_-) = q^0 g^{-1}\sum_p t(p_-)t(p_+)G_0(p-k). \tag{E11}$$

Combining Eqs. (E10) and (E11) then produces

$$q_\mu\big[\mathrm{AL}^{\mu}_{\mathrm{H},1}(k_+,k_-) + \mathrm{AL}^{\mu}_{\mathrm{H},2}(k_+,k_-) + \lambda^{\mu}_{\mathrm{H}}(k_+,k_-)\big] = \sum_p G_0(p-k)[t(p_-)(p_+)^0 - t(p_+)(p_-)^0]. \tag{E12}$$

Adding Eq. (E7) together with Eq. (E12) and simplifying gives

$$q_\mu\left[\mathrm{MT}^\mu_{\mathrm{H}}(k_+,k_-)+\mathrm{AL}^\mu_{\mathrm{H},1}(k_+,k_-)+\mathrm{AL}^\mu_{\mathrm{H},2}(k_+,k_-)+\lambda^\mu_{\mathrm{H}}(k_+,k_-)\right]=\sum_p G_0(p-k)[t(p_-)(k_+)^0-t(p_+)(k_-)^0]$$
$$=(k_+)^0\Sigma(k_-)-(k_-)^0\Sigma(k_+). \tag{E13}$$

The contraction of the full heat vertex is thus

$$q_\mu\Gamma^\mu_{\mathrm{H}}(k_+,k_-)=q_\mu\left[\gamma^\mu_{\mathrm{H}}(k_+,k_-)+\mathrm{MT}^\mu_{\mathrm{H}}(k_+,k_-)+\mathrm{AL}^\mu_{\mathrm{H},1}(k_+,k_-)+\mathrm{AL}^\mu_{\mathrm{H},2}(k_+,k_-)+\lambda^\mu_{\mathrm{H}}(k_+,k_-)\right]$$
$$=(k_-)^0G_0^{-1}(k_+)-(k_+)^0G_0^{-1}(k_-)+(k_+)^0\Sigma(k_-)-(k_-)^0\Sigma(k_+)$$
$$=(k_-)^0G^{-1}(k_+)-(k_+)^0G^{-1}(k_-). \tag{E14}$$

As claimed in Sec. VI of the main text, the full heat vertex in Eq. (E1) satisfies the WTI for energy conservation [Eq. (E6)]. Note that it is crucial to include the vertex $\lambda^\mu_{\mathrm{H}}(k_+,k_-)$ to satisfy the WTI.

2. Bosonic electromagnetic vertex

This section presents a derivation of the bosonic electromagnetic vertex appearing in the Aslamazov-Larkin diagrams. The derivation is based solely on the form of the "triangle" vertices appearing in these diagrams, along with the constraint imposed by the Ward-Takahashi identity. Without loss of generality, consider the $\hat{x}$ component. Equivalent results hold for the $\hat{y}$ and $\hat{z}$ components. This vertex appears in Eq. (5.2) of the main text.

The electromagnetic "triangle" vertex appearing in the $\mathrm{AL}^x_{\mathrm{E},1}$ diagram is shown in Fig. 13. Mathematically this is given by

$$\Lambda^x_{\mathrm{E},1}(p,p)=-\sum_l G_0(p-l)G(l)\Gamma^x_{\mathrm{E}}(l,l)G(l). \tag{E15}$$

The minus sign arises from the fermion loop in the Aslamazov-Larkin triangle vertex. The WTI for global particle number conservation is $q_\mu\Gamma^\mu_{\mathrm{E}}(k_+,k_-)=G^{-1}(k_+)-G^{-1}(k_-)$. In the $q\to 0$ limit, this produces the Ward identity: $\Gamma^\mu_{\mathrm{E}}(k,k)=\partial G^{-1}(k)/\partial k_\mu$. For the $\hat{x}$ component, it follows that $\Gamma^x_{\mathrm{E}}(l,l)=-\partial G^{-1}(l)/\partial l^x$. Inserting this into Eq. (E15) and then performing integration by parts gives

$$\Lambda^x_{\mathrm{E},1}(p,p)=\sum_l G_0(p-l)G(l)\frac{\partial G^{-1}(l)}{\partial l^x}G(l)$$
$$=-\sum_l G_0(p-l)\frac{\partial G(l)}{\partial l^x}$$
$$=\sum_l \frac{\partial G_0(p-l)}{\partial l^x}G(l)$$
$$=-\frac{\partial}{\partial p^x}\sum_l G_0(p-l)G(l). \tag{E16}$$

By definition, the pair susceptibility is $\Pi(p)=\sum_l G_0(p-l)G(l)=t^{-1}(p)-g^{-1}$. Therefore, it follows that the bosonic electromagnetic vertex for $\mathrm{AL}^x_{\mathrm{E},1}$ is

$$\Lambda^x_{\mathrm{E},1}(p,p)=-\frac{\partial\Pi(p)}{\partial p^x}=-\frac{\partial t^{-1}(p)}{\partial p^x}. \tag{E17}$$

For comparison, the fermionic electromagnetic vertex, derived above, is $\Gamma^x_{\mathrm{E}}(k,k)=-\partial G^{-1}(k)/\partial k^x$.

The electromagnetic vertex appearing in the $\mathrm{AL}^x_{\mathrm{E},2}$ diagram is derived in exactly the same manner. This diagram is shown in Fig. 14. Mathematically this is given by

$$\Lambda^x_{\mathrm{E},2}(p,p)=-\sum_l G(p-l)G_0(l)\gamma^x_{\mathrm{E}}(l,l)G_0(l). \tag{E18}$$

The minus sign arises from the fermion loop in the Aslamazov-Larkin triangle vertex. Following the same steps as before, this vertex can be simplified as follows:

$$\Lambda^x_{\mathrm{E},2}(p,p)=\sum_l G(p-l)G_0(l)\frac{\partial G_0^{-1}(l)}{\partial l^x}G_0(l)$$
$$=-\sum_l G(p-l)\frac{\partial G_0(l)}{\partial l^x}$$

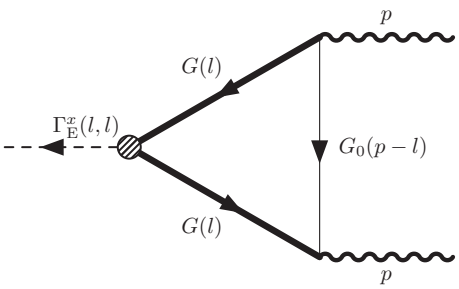

FIG. 13. The electromagnetic "triangle" vertex appearing in the $\mathrm{AL}^x_{\mathrm{E},1}$ Aslamazov-Larkin diagram. The external momentum p is the momentum of the pair propagators. The triangle vertex represents a bosonic electromagnetic vertex, $\Lambda^x_{\mathrm{E},1}(p,p)$, which is computed in the text.

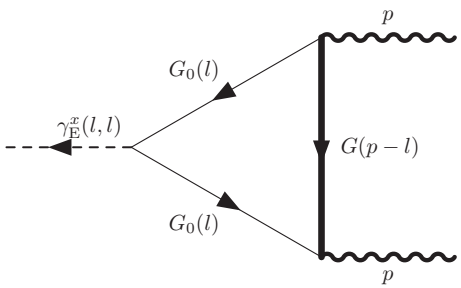

FIG. 14. The electromagnetic "triangle" vertex appearing in the $\mathrm{AL}^x_{\mathrm{E},2}$ Aslamazov-Larkin diagram. The external momentum p is the momentum of the pair propagators. The triangle vertex represents a bosonic electromagnetic vertex, $\Lambda^x_{\mathrm{E},2}(p,p)$, which is computed in the text.

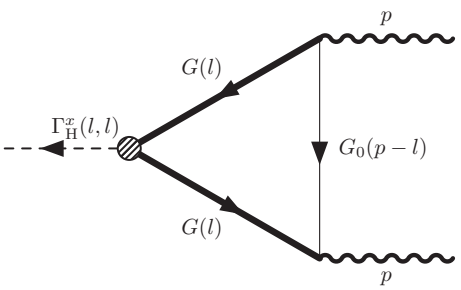

FIG. 15. The heat "triangle" vertex appearing in the $\mathrm{AL}^x_{\mathrm{H},1}$ Aslamazov-Larkin diagram. The external momentum p is the momentum of the pair propagators. The triangle vertex represents a bosonic heat vertex $\Lambda^x_{\mathrm{H},1}(p,p)$, which is computed in the text.

$$= \sum_l \frac{\partial G(p-l)}{\partial l^x} G_0(l)$$

$$= -\frac{\partial}{\partial p^x} \sum_l G(p-l) G_0(l). \tag{E19}$$

The pair susceptibility can also be written as $\Pi(p) = \sum_l G(p-l)G_0(l) = t^{-1}(p) - g^{-1}$. Therefore, it follows that the bosonic electromagnetic vertex for $\mathrm{AL}^x_{\mathrm{E},2}$ is

$$\Lambda^x_{\mathrm{E},2}(p,p) = -\frac{\partial \Pi(p)}{\partial p^x} = -\frac{\partial t^{-1}(p)}{\partial p^x}. \tag{E20}$$

Thus, the bosonic electromagnetic vertex appearing in $\mathrm{AL}^x_{\mathrm{E},1}$ and $\mathrm{AL}^x_{\mathrm{E},2}$ is identical: $\Lambda^x_{\mathrm{E},1}(p,p) = \Lambda^x_{\mathrm{E},2}(p,p)$. It follows that the bosonic EM vertex for the combination of $\mathrm{AL}^x_{\mathrm{E},1} + \mathrm{AL}^x_{\mathrm{E},2}$ is

$$\Lambda^x_{\mathrm{E},1}(p,p) + \Lambda^x_{\mathrm{E},2}(p,p) \equiv \Lambda^x_{\mathrm{E}}(p,p) = -2\frac{\partial \Pi(p)}{\partial p^x}$$

$$= -2\frac{\partial t^{-1}(p)}{\partial p^x}. \tag{E21}$$

3. Bosonic heat vertex

The form of the bosonic heat vertex requires a more lengthy analysis, which is presented in what follows. Without loss of generality, consider the $\hat{x}$ component. Equivalent results hold for the $\hat{y}$ and $\hat{z}$ components. The heat "triangle" vertex for the $\mathrm{AL}^x_{\mathrm{H},1}$ Aslamazov-Larkin diagram is shown in Fig. 15. Mathematically this is given by

$$\Lambda^x_{\mathrm{H},1}(p,p) = -\sum_l G_0(p-l)G(l)\Gamma^x_{\mathrm{H}}(l,l)G(l). \tag{E22}$$

The minus sign arises from the fermion loop in the Aslamazov-Larkin triangle vertex. The WTI for global spacetime translation symmetry (conservation of energy) is $q_\mu \Gamma^\mu_{\mathrm{H}}(k_+,k_-) = \omega_- G^{-1}(k_+) - \omega_+ G^{-1}(k_-)$. In the $q \to 0$ limit, this gives the heat vertex analog of the EM Ward identity. For the $\hat{x}$ component, it follows that $\Gamma^x_{\mathrm{H}}(l,l) = -\epsilon[\partial G^{-1}(l)/\partial l^x]$. Inserting this into Eq. (E22), and then performing integration by parts, gives

$$\Lambda^x_{\mathrm{H},1}(p,p) = \sum_l i\epsilon_n G_0(p-l)G(l)\frac{\partial G^{-1}(l)}{\partial l^x} G(l)$$

$$= -\sum_l i\epsilon_n G_0(p-l)\frac{\partial G(l)}{\partial l^x}$$

$$= \sum_l i\epsilon_n \frac{\partial G_0(p-l)}{\partial l^x} G(l)$$

$$= -\frac{\partial}{\partial p^x}\sum_l i\epsilon_n G_0(p-l)G(l). \tag{E23}$$

Now write this in a symmetric form, by letting $l \to l + p/2$, and also $l \to -l + p/2$, and summing one half of each of the resulting expressions; this produces

$$\Lambda^x_{\mathrm{H},1}(p,p) = -\frac{1}{2}\frac{\partial}{\partial p^x}\sum_l (i\epsilon_n + i\varpi_m/2)G_0(p/2-l)G(l+p/2)$$

$$-\frac{1}{2}\frac{\partial}{\partial p^x}\sum_l (-i\epsilon_n + i\varpi_m/2)G_0(p/2+l)G(-l+p/2). \tag{E24}$$

The heat "triangle" vertex for the $\mathrm{AL}^x_{\mathrm{H},2}$ Aslamazov-Larkin diagram is shown in Fig. 16. Mathematically this is given by

$$\Lambda^x_{\mathrm{H},2}(p,p) = -\sum_l G(p-l)G_0(l)\gamma^x_{\mathrm{H}}(l,l)G_0(l). \tag{E25}$$

The minus sign arises from the fermion loop in the Aslamazov-Larkin triangle vertex. Following the same steps as before, this vertex can be simplified as follows:

$$\Lambda^x_{\mathrm{H},2}(p,p) = \sum_l i\epsilon_n G(p-l)G_0(l)\frac{\partial G_0^{-1}(l)}{\partial l^x} G_0(l)$$

$$= -\sum_l i\epsilon_n G(p-l)\frac{\partial G_0(l)}{\partial l^x}$$

$$= \sum_l i\epsilon_n \frac{\partial G(p-l)}{\partial l^x} G_0(l)$$

$$= -\frac{\partial}{\partial p^x}\sum_l i\epsilon_n G(p-l)G_0(l). \tag{E26}$$

Now write this in a symmetric form, by letting $l \to l + p/2$, and also $l \to -l + p/2$, and summing one half of each of the resulting expressions; this produces

$$\Lambda^x_{\mathrm{H},2}(p,p) = -\frac{1}{2}\frac{\partial}{\partial p^x}\sum_l (i\epsilon_n + i\varpi_m/2)G(p/2-l)G_0(l+p/2) - \frac{1}{2}\frac{\partial}{\partial p^x}\sum_l (-i\epsilon_n + i\varpi_m/2)G(p/2+l)G_0(-l+p/2). \tag{E27}$$

Adding the results in Eqs. (E24) and (E27) together and simplifying then produces

$$\begin{aligned}\Lambda^x_{\mathrm{H},1}(p,p) + \Lambda^x_{\mathrm{H},2}(p,p) &\equiv \Lambda^x_{\mathrm{H}}(p,p) = -\frac{i\varpi_m}{2}\frac{\partial}{\partial p^x}\sum_l G_0(p/2-l)G(l+p/2) \\ &\quad - \frac{i\varpi_m}{2}\frac{\partial}{\partial p^x}\sum_l G_0(p/2+l)G(-l+p/2) \\ &= -i\varpi_m\frac{\partial}{\partial p^x}\sum_l G_0(p-l)G(l). \end{aligned}\tag{E28}$$

Using the definition of the pair susceptibility, $\Pi(p) = \sum_l G_0(p-l)G(l) = t^{-1}(p) - g^{-1}$, it follows that the bosonic heat vertex for the combination of $\mathrm{AL}^x_{\mathrm{H},1} + \mathrm{AL}^x_{\mathrm{H},2}$ is

$$\begin{aligned}\Lambda^x_{\mathrm{H},1}(p,p) + \Lambda^x_{\mathrm{H},2}(p,p) \equiv \Lambda^x_{\mathrm{H}}(p,p) &= -\varpi\frac{\partial\Pi(p)}{\partial p^x} \\ &= -\varpi\frac{\partial t^{-1}(p)}{\partial p^x}. \end{aligned}\tag{E29}$$

For comparison, the fermionic full heat vertex, derived above, is $\Gamma^x_{\mathrm{H}}(k,k) = -\omega[\partial G^{-1}(k)/\partial k^x]$. Notice that it is the sum of two heat triangle vertices which produces a bosonic heat vertex in a form similar to its fermionic counterpart. This factor of two has caused a lot of controversy in the literature [21,28,44–46]. The factor of two difference between the fermionic and bosonic result is due to charge, as will be explained in detail in the next paragraph.

If we restore the electric charge e appearing in the EM vertex, then the relation between the fermionic heat and EM vertices is

$$\Gamma^x_{\mathrm{H}}(k,k) = \frac{\omega}{e}\Gamma^x_{\mathrm{E}}(k,k). \tag{E30}$$

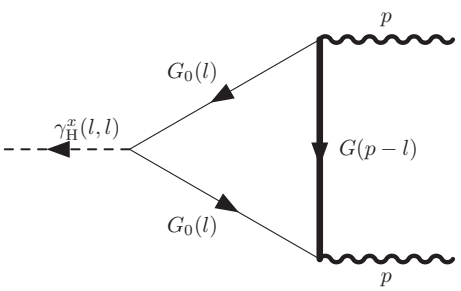

FIG. 16. The heat "triangle" vertex for the $\mathrm{AL}^x_{\mathrm{H},2}$ Aslamazov-Larkin diagram. The external momentum p is the momentum of the pair propagators. The triangle vertex represents a bosonic heat vertex $\Lambda^x_{\mathrm{H},2}(p,p)$, which is computed in the text.

The bosonic heat vertex Λ^x_{H} is defined by $\Lambda^x_{\mathrm{H},1}(p,p) + \Lambda^x_{\mathrm{H},2}(p,p) \equiv \Lambda^x_{\mathrm{H}}(p,p) = \varpi[\partial\Pi(p)/\partial p^x] = \varpi[\partial t^{-1}(p)/\partial p^x]$. Similarly the bosonic EM vertex Λ^x_{E} obeys $\Lambda^x_{\mathrm{E},1}(p,p) + \Lambda^x_{\mathrm{E},2}(p,p) \equiv \Lambda^x_{\mathrm{E}}(p,p) = 2[\partial\Pi(p)/\partial p^x] = 2[\partial t^{-1}(p)/\partial p^x]$. Thus, the relation between the bosonic heat and EM vertices is

$$\Lambda^x_{\mathrm{H}}(p,p) = \frac{\varpi}{2e}\Lambda^x_{\mathrm{E}}(p,p) = \frac{\varpi}{e^*}\Lambda^x_{\mathrm{E}}(p,p). \tag{E31}$$

Here $e^* = 2e$, and the factor of two appears due to the composite bosons comprising of paired fermions. Thus, the fundamental relation between the heat and EM vertices is that the heat vertex equals the matter current multiplied by energy (frequency) whereas the EM vertex equals the matter current multiplied by charge; thus the heat vertex equals the EM vertex multiplied by the ratio of frequency to charge. The normalization by the corresponding charge (e for fermions and e^* for bosons) causes there to be a factor of two difference between microscopic fermions and composite bosons, because the composite bosons are formed from the pairing of two fermions and thus have charge $e^* = 2e$ [37]. This result has also been derived independently in Ref. [55].

4. Transverse thermoelectric coefficient

The result for the transverse thermoelectric coefficient is given in Eq. (6.11) of the main text. Here further details of the calculation are presented. As stated in Sec. VI of the main text, the transverse thermoelectric coefficient is computed by performing all possible electromagnetic vertex insertions in the heat current–electric current correlation function. In the small-$|\mu_{\mathrm{pair}}|$ limit, only the electromagnetic vertex insertions in the Aslamazov-Larkin diagram contribution to this correlation function are of interest [21]. The reason for this is similar to what occurs in the case of the diamagnetic susceptibility, which in the small-$|\mu_{\mathrm{pair}}|$ limit has a singular contribution arising from only the Aslamazov-Larkin diagrams. Finally, only the electromagnetic vertex insertions in the pair propagator need to be considered. Again, the resulting correlation function gives the most singular contribution because it contains three pair propagators [21]. For a given pair propagator, there are two electromagnetic triangle vertices that can be inserted into the propagator. Since the $\mathrm{AL}^x_{\mathrm{E},1}$ and $\mathrm{AL}^x_{\mathrm{E},2}$ electromagnetic vertices are equivalent to the bosonic electromagnetic vertex $\Lambda^x_{\mathrm{E},1}$ [see Eqs. (E17) and (E20)], these two insertions give a symmetry factor of two. There is also the symmetry factor of two arising from spin degeneracy for a spin-$\frac{1}{2}$ system of fermions. Finally, the heat vertex for the combination of $\mathrm{AL}^y_{\mathrm{H},1}$ and $\mathrm{AL}^y_{\mathrm{H},2}$ reduces to the bosonic heat vertex Λ^y_{H}.

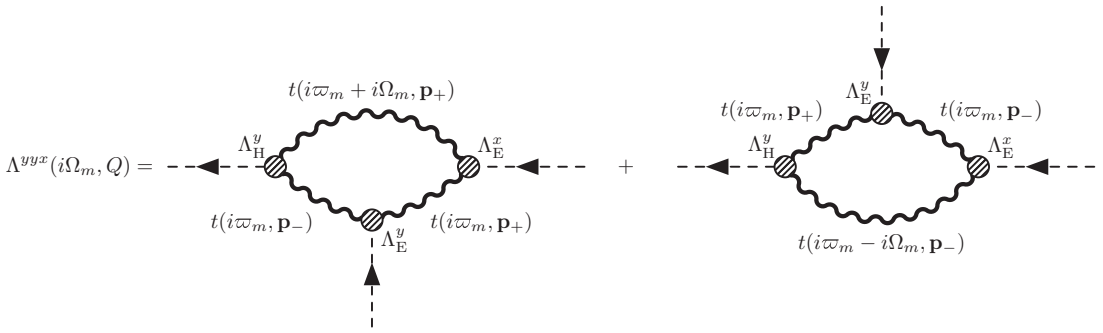

FIG. 17. The Aslamazov-Larkin diagrams that give the singular contribution to the transverse thermoelectric coefficient. The vertices $\Lambda_{\rm E}$ and $\Lambda_{\rm H}$ represent bosonic electromagnetic and heat vertices, respectively. The bosonic vertices have been computed in Appendix E2 and Appendix E3 from the triangle vertices in the Aslamazov-Larkin diagrams.

Thus, the bosonic three-point correlation function has a total symmetry factor of four. This symmetry factor of four can be absorbed into the EM vertices using $\Lambda_{\rm E} = 2\Lambda_{\rm E,1}$. The correlation function now becomes

$$\begin{aligned}\Lambda^{yyx}(i\Omega_m, Q) = &-e^2 \sum_p \big[\Lambda^y_{\rm H}(i\varpi_m + i\Omega_m, \mathbf{p}_+; i\varpi_m, \mathbf{p}_-)\Lambda^y_{\rm E}(i\varpi_m, \mathbf{p}_-; i\varpi_m, \mathbf{p}_+)\Lambda^x_{\rm E}(i\varpi_m, \mathbf{p}_+; i\varpi_m + i\Omega_m, \mathbf{p}_+) \\ &\times t(i\varpi_m + i\Omega_m, \mathbf{p}_+)t(i\varpi_m, \mathbf{p}_-)t(i\varpi_m, \mathbf{p}_+) \\ &+ \Lambda^y_{\rm H}(i\varpi_m - i\Omega_m, \mathbf{p}_-; i\varpi_m, \mathbf{p}_+)\Lambda^y_{\rm E}(i\varpi_m, \mathbf{p}_+; i\varpi_m, \mathbf{p}_-)\Lambda^x_{\rm E}(i\varpi_m, \mathbf{p}_-; i\varpi_m - i\Omega_m, \mathbf{p}_-) \\ &\times t(i\varpi_m - i\Omega_m, \mathbf{p}_-)t(i\varpi_m, \mathbf{p}_+)t(i\varpi_m, \mathbf{p}_-)\big]. \end{aligned} \tag{E32}$$

Here the vertex notation is defined by $\Lambda^x(p + Q + i\Omega_m, p) \equiv \Lambda^x(i\varpi_m + i\Omega_m, \mathbf{p} + \mathbf{Q}; i\varpi_m, \mathbf{p})$, and $\mathbf{p}_\pm \equiv \mathbf{p} \pm \mathbf{Q}/2$. The vector $\mathbf{Q}$ is along the $\hat{x}$ direction: $\mathbf{Q} = Q\hat{\mathbf{x}}$. The diagrams for this bosonic three-point correlation function are shown in Fig. 17.

The bosonic electromagnetic and heat vertices are given in Eqs. (E21) and (E29), respectively. Using these results to express the bosonic vertices in Eq. (E32) then gives

$$\begin{aligned}\Lambda^{yyx}(i\Omega_m, Q) = -4e^2 \sum_p \Bigg[&\frac{Zp^x_+}{M_{\rm pair}}\left(\frac{Zp^y}{M_{\rm pair}}\right)^2 (i\varpi_m + i\Omega_m/2)t(i\varpi_m + i\Omega_m, \mathbf{p}_+)t(i\varpi_m, \mathbf{p}_-)t(i\varpi_m, \mathbf{p}_+) \\ &+ \frac{Zp^x_-}{M_{\rm pair}}\left(\frac{Zp^y}{M_{\rm pair}}\right)^2 (i\varpi_m - i\Omega_m/2)t(i\varpi_m - i\Omega_m, \mathbf{p}_-)t(i\varpi_m, \mathbf{p}_+)t(i\varpi_m, \mathbf{p}_-)\Bigg]. \end{aligned} \tag{E33}$$

The Matsubara frequency summation is performed by using the Eliashberg contour [5,21,32] (see Appendix C for details). After performing the Matsubara frequency summation, and analytically continuing to real frequencies, $i\Omega_m \to \Omega + i0^+$, the result is

$$\begin{aligned}\Lambda^{yyx}(\Omega, Q) = -4e^2 \sum_{\mathbf{p}} \int_{-\infty}^{\infty} \frac{dx}{2\pi} \coth\left(\frac{1}{2}\beta x\right) \Bigg\{ &\frac{Zp^x_+}{M_{\rm pair}}\left(\frac{Zp^y}{M_{\rm pair}}\right)^2 (x + \Omega/2)t_{\rm R}(x + \Omega, \mathbf{p}_+)\mathrm{Im}[t_{\rm R}(x, \mathbf{p}_-)t_{\rm R}(x, \mathbf{p}_+)] \\ &+ \frac{Zp^x_+}{M_{\rm pair}}\left(\frac{Zp^y}{M_{\rm pair}}\right)^2 (x - \Omega/2)t_{\rm A}(x - \Omega, \mathbf{p}_+)t_{\rm A}(x - \Omega, \mathbf{p}_-)\mathrm{Im}[t_{\rm R}(x, \mathbf{p}_+)] \\ &+ \frac{Zp^x_-}{M_{\rm pair}}\left(\frac{Zp^y}{M_{\rm pair}}\right)^2 (x - \Omega/2)t_{\rm A}(x - \Omega, \mathbf{p}_-)\mathrm{Im}[t_{\rm R}(x, \mathbf{p}_+)t_{\rm R}(x, \mathbf{p}_-)] \\ &+ \frac{Zp^x_-}{M_{\rm pair}}\left(\frac{Zp^y}{M_{\rm pair}}\right)^2 (x + \Omega/2)t_{\rm R}(x + \Omega, \mathbf{p}_-)t_{\rm R}(x + \Omega, \mathbf{p}_+)\mathrm{Im}[t_{\rm R}(x, \mathbf{p}_-)]\Bigg\}. \end{aligned} \tag{E34}$$

The transverse thermoelectric coefficient can now be computed using the Kubo formula:

$$\frac{j_y}{EB} = -\lim_{\Omega, Q \to 0} \frac{1}{\Omega Q c} \mathrm{Re}[\Lambda^{yyx}(\Omega, Q)|_{i\Omega_m \to \Omega + i0^+}]. \tag{E35}$$

Inserting the retarded pair propagator, defined by $t_{\rm R}^{-1}(x, \mathbf{p}) = Z[\kappa x - \mathbf{p}^2/(2M_{\rm pair}) - |\mu_{\rm pair}| + i\Gamma x]$, into Eq. (E34), and then taking the limits $Q \to 0$ followed by $\Omega \to 0$ in Eq. (E35), gives j_y/EB. In the small-$|\mu_{\rm pair}|$ limit, the main contribution to the integral occurs when $\beta x \ll 1$, which allows the coth function to be expanded as $\coth(\beta x/2) \approx 2T/x$. In this limit, the current

becomes

$$\begin{aligned}\frac{j_y}{EB} &= \frac{4Te^2}{c}\sum_{\mathbf{p}}\left(\frac{Zp^x}{M_{\rm pair}}\right)^2\left(\frac{Zp^y}{M_{\rm pair}}\right)^2\int_{-\infty}^{\infty}\frac{dx}{\pi}\frac{1}{x}\{{\rm Re}[t_{\rm R}^3(x,\mathbf{p})]{\rm Im}[t_{\rm R}(x,\mathbf{p})]-{\rm Im}[t_{\rm R}^3(x,\mathbf{p})]{\rm Re}[t_{\rm R}(x,\mathbf{p})]\}\\ &= \frac{4Te^2}{c}\sum_{\mathbf{p}}\left(\frac{p^x}{M_{\rm pair}}\right)^2\left(\frac{p^y}{M_{\rm pair}}\right)^2\int_{-\infty}^{\infty}\frac{dx}{\pi}\frac{1}{x}\frac{2\Gamma x(\kappa x-\mathbf{p}^2/2M_{\rm pair}-|\mu_{\rm pair}|)}{\{[\kappa x-\mathbf{p}^2/(2M_{\rm pair})-|\mu_{\rm pair}|]^2+(\Gamma x)^2\}^3}\\ &= \frac{-3Te^2}{c}\left(\frac{\kappa^2+\Gamma^2}{\Gamma^2}\right)\sum_{\mathbf{p}}\left(\frac{p^x}{M_{\rm pair}}\right)^2\left(\frac{p^y}{M_{\rm pair}}\right)^2\frac{1}{[\mathbf{p}^2/(2M_{\rm pair})+|\mu_{\rm pair}|]^4}\\ &= \frac{-2Te^2}{c}\left(\frac{\kappa^2+\Gamma^2}{\Gamma^2}\right)\sum_{\mathbf{p}}\frac{1}{(\mathbf{p}^2+2M_{\rm pair}|\mu_{\rm pair}|)^2}.\end{aligned}\tag{E36}$$

The momentum integral is the same as that performed in Eq. (C9). Using that result for the momentum integration then gives the result in Eq. (6.10) of the main text:

$$\frac{j_y}{EB} = -\frac{k_BTe^2}{4\pi\hbar^2c}\sqrt{\frac{1/(2M_{\rm pair})}{|\mu_{\rm pair}|}}\left(\frac{\kappa^2+\Gamma^2}{\Gamma^2}\right).\tag{E37}$$

The constants $\hbar$, k_B, and c have been restored in this expression. The transverse thermoelectric coefficient is determined from $\widetilde{\alpha}_{xy} = B[c\chi_{\rm dia}/\hbar - j^y/(EB)]$; using Eqs. (C10) and (E37) then gives the result stated in Eq. (6.11) of the main text:

$$\widetilde{\alpha}_{xy} = \frac{Bk_BTe^2}{12\pi\hbar^2c}\sqrt{\frac{1/(2M_{\rm pair})}{|\mu_{\rm pair}|}}\left(\frac{3\kappa^2+\Gamma^2}{\Gamma^2}\right).\tag{E38}$$

[1] B. Keimer, S. Kivelson, M. Norman, S. Uchida, and J. Zaanen, Nature (London) **518**, 179 (2015).

[2] G. Ghiringhelli, M. L. Tacon, M. Minola, S. Blanco-Canosa, C. Mazzoli, N. B. Brookes, G. M. D. Luca, A. Frano, D. G. Hawthorn, F. He, T. Loew, M. M. Sala, D. C. Peets, M. Salluzzo, E. Schierle, R. Sutarto, G. A. Sawatzky, E. Weschke, B. Keimer, and L. Braicovich, Science **337**, 821 (2012).

[3] R. Comin, R. Sutarto, F. He, E. H. da Silva Neto, L. Chauviere, A. Frano, R. Liang, W. N. Hardy, D. A. Bonn, Y. Yoshida, H. Eisaki, A. J. Achkar, D. G. Hawthorn, B. Keimer, G. A. Sawatzky, and A. Damascelli, Nat. Mater. **14**, 796 (2015).

[4] T. Wu, H. Mayaffre, S. Kramer, M. Horvatic, C. Berthier, W. Hardy, R. Liang, D. Bonn, and M.-H. Julien, Nature (London) **477**, 191 (2011).

[5] A. Larkin and A. Varlamov, *Theory of Fluctuations in Superconductors*, International Series of Monographs on Physics (Oxford University Press, Oxford, 2009).

[6] Z. A. Xu, N. P. Ong, Y. Wang, S. Kakeshita, and T. Uchida, Nature (London) **406**, 486 (2000).

[7] L. Li, Y. Wang, S. Komiya, S. Ono, Y. Ando, G. D. Gu, and N. P. Ong, Phys. Rev. B **81**, 054510 (2010).

[8] Q. J. Chen, I. Kosztin, B. Jankó, and K. Levin, Phys. Rev. B **59**, 7083 (1999).

[9] Q. J. Chen, J. Stajic, S. N. Tan, and K. Levin, Phys. Rep. **412**, 1 (2005).

[10] Q. J. Chen and J. B. Wang, Front. Phys. **9**, 539 (2014).

[11] A. J. Leggett, in *Modern Trends in the Theory of Condensed Matter* (Springer-Verlag, Berlin, 1980), pp. 13–27.

[12] A. J. Leggett, Nat. Phys. **2**, 134 (2006).

[13] There has been some misunderstanding that applying the BCS-BEC crossover picture to the cuprates implies a negative fermionic chemical potential. We emphasize that this is not true. In fact, the BEC regime cannot be reached in d-wave superconductors except at unphysical small electron densities, as discussed in Ref. [8].

[14] Y. Y. Wang, L. Li, and N. P. Ong, Phys. Rev. B **73**, 024510 (2006).

[15] F. Yu, M. Hirschberger, T. Loew, G. Li, B. J. Lawson, T. Asaba, J. B. Kemper, T. Liang, J. Porras, G. S. Boebinger, J. Singleton, B. Keimer, L. Li, and N. P. Ong, Proc. Natl. Acad. Sci. USA **113**, 12667 (2016).

[16] J. Chang, R. Daou, C. Proust, D. LeBoeuf, N. Doiron-Leyraud, F. Laliberté, B. Pingault, B. J. Ramshaw, R. Liang, D. A. Bonn, W. N. Hardy, H. Takagi, A. B. Antunes, I. Sheikin, K. Behnia, and L. Taillefer, Phys. Rev. Lett. **104**, 057005 (2010).

[17] X. Yang and C. Nayak, Phys. Rev. B **65**, 064523 (2002).

[18] B. R. Patton, The Effect of fluctuations in superconducting alloys above the transition temperature, Ph.D. thesis, Cornell University, 1971.

[19] K. Behnia and H. Aubin, Rep. Prog. Phys. **79**, 046502 (2016).

[20] L. G. Aslamazov and A. I. Larkin, Sov. Phys. JETP **40**, 321 (1975).

[21] I. Ussishkin, Phys. Rev. B **68**, 024517 (2003).

[22] I. Ussishkin, S. L. Sondhi, and D. A. Huse, Phys. Rev. Lett. **89**, 287001 (2002).

[23] D. Podolsky, S. Raghu, and A. Vishwanath, Phys. Rev. Lett. **99**, 117004 (2007).

[24] I. Ussishkin and S. L. Sondhi, Int. J. Mod. Phys. B **18**, 3315 (2004).

[25] X. Jiang, D. Li, and B. Rosenstein, Phys. Rev. B **89**, 064507 (2014).

[26] J. Stajic, A. Iyengar, Q. J. Chen, and K. Levin, Phys. Rev. B **68**, 174517 (2003).

[27] J. Maly, B. Jankó, and K. Levin, Physica C **321**, 113 (1999).

[28] A. Levchenko, M. R. Norman, and A. A. Varlamov, Phys. Rev. B **83**, 020506 (2011).

[29] D. Wulin and K. Levin, Phys. Rev. B **86**, 184513 (2012).

[30] S. Tan and K. Levin, Phys. Rev. B **69**, 064510 (2004).

[31] To uniquely fix the prefactor Z of the pair propagator, we take $\kappa = 1$. In the exact particle-hole symmetric limit, where $\kappa = 0$, this prefactor can be determined from weak-fluctuation theory [5]. For quasi-two-dimensional cuprates the pair dispersion can be written as $\Omega_{\mathbf{q}} = \mathbf{q}_{\|}^2/(2M_{\|}) + \mathbf{q}_{\perp}^2/(2M_{\perp}) - \mu_{\rm pair}$, where $\|$ ($\perp$) denotes the in-plane (out-of-plane) component. For further discussion of these parameters see Refs. [9,10].

[32] G. D. Mahan, *Many-Particle Physics*, 2nd ed. (Plenum Press, New York, 1990).

[33] L. P. Kadanoff and P. C. Martin, Phys. Rev. **124**, 670 (1961).

[34] Q. J. Chen, Generalization of BCS theory to short coherence length superconductors: A BCS-Bose-Einstein crossover scenario, Ph.D. thesis, University of Chicago, 2000.

[35] N. M. Hugenholtz and D. Pines, Phys. Rev. **116**, 489 (1959).

[36] J. R. Schrieffer, *Theory of Superconductivity*, 3rd ed. (The Benjamin/Cummings Inc., Reading, MA, 1983).

[37] In the expression given for the response function, the electron charge e has been explicitly incorporated [see Eq. (3.1)]. Thus, the full vertex $\Gamma_{\rm E}^{\mu}(k_+,k_-)$ is in fact the matter-current vertex. Technically the EM vertex is given by $e\Gamma_{\rm E}^{\mu}(k_+,k_-)$. It is convenient to explicitly put the charge in the response function; however, one must then be aware that when we refer to the "EM" vertex $\Gamma_{\rm E}^{\mu}$ it is in fact the matter-current vertex. When the heat vertex $\Gamma_{\rm H}^{\mu}$ is also considered, the relation $\Gamma_{\rm H}^{y}(k,k) = \omega\Gamma_{\rm E}^{y}(k,k)$ states that the heat-current vertex is equal to energy multiplied by the matter-current vertex. Combining these two relations, it follows that the relation between the heat-current vertex and the real EM vertex is thus $\Gamma_{\rm H}^{y}(k,k) = (\omega/e)\Gamma_{\rm E}^{y}(k,k)$. Incorporating the charge here is important, due to factors of two that have caused confusion in the literature. For fermions it is found that $\Gamma_{\rm H}^{y}(k,k) = (\omega/e)\Gamma_{\rm E}^{y}(k,k)$, whereas for the composite bosons considered in this work $\Lambda_{\rm H}^{y}(p,p) = (\varpi/e^*)\Lambda_{\rm E}^{y}(p,p)$, where $e^* = 2e$. The relation between the heat-current vertex and the electromagnetic-current vertex is thus a universal relation; however, the explicit charge appearing in this relation is dependent on the particle constituents, i.e., whether they are fundamental particles or composite particles.

[38] L. H. Ryder, *Quantum Field Theory*, 2nd ed. (Cambridge University Press, Cambridge, UK, 1996).

[39] G. Vignale, M. Rasolt, and D. J. W. Geldart, Phys. Rev. B **37**, 2502 (1988).

[40] K. Maki, Prog. Theor. Phys. **40**, 193 (1968).

[41] L. G. Aslamazov and A. I. Larkin, Sov. Phys. Solid State **10**, 875 (1968).

[42] We have presented the G_0G_0 pair-fluctuation theory as an analog of the GG_0 theory, but with two bare Green's functions in the pair susceptibility. Thus, the self-energy has the form $\Sigma = t_0G_0$. However, in the conventional weak-fluctuation literature [5], this physics is derived from Gaussian fluctuations in the path integral. In this approach there is no self-energy; the mean field is fixed at the BCS level and one can consider Gaussian fluctuations about the saddle-point action. These modify the EM response and will give exactly bare MT+DOS+AL diagrams. However, if one has a theory with a self-energy $\Sigma = t_0G_0$, then the response will not be just bare MT+DOS+AL diagrams; these will be the response to lowest order.

[43] It is important to note, however, that the MT contribution cannot always be ignored. Indeed, as shown originally by Maki [40], the MT diagram gives a contribution to the conductivity of the same order as the AL diagrams [5]. In fact, as Thompson [61] showed, without accounting for pair-breaking processes the MT diagram gives a divergent contribution to the two-dimensional electrical conductivity [5]. The anomalous Maki-Thompson contribution to transport coefficients arises when considering the finite-frequency response. However, since diamagnetic susceptibility is a static response, this term does not arise when calculating this particular transport coefficient.

[44] M. Y. Reizer and A. V. Sergeev, Phys. Rev. B **50**, 9344 (1994).

[45] A. Sergeev, M. Y. Reizer, and V. Mitin, Phys. Rev. B **77**, 064501 (2008).

[46] M. N. Serbyn, M. A. Skvortsov, A. A. Varlamov, and V. Galitski, Phys. Rev. Lett. **102**, 067001 (2009).

[47] Y. He and K. Levin, Phys. Rev. B **89**, 035106 (2014).

[48] B. L. Altshuler, D. Khmel'nitzkii, A. I. Larkin, and P. A. Lee, Phys. Rev. B **22**, 5142 (1980).

[49] N. R. Cooper, B. I. Halperin, and I. M. Ruzin, Phys. Rev. B **55**, 2344 (1997).

[50] A. Sergeev, M. Reizer, and V. Mitin, Phys. Rev. Lett. **106**, 139701 (2011).

[51] M. N. Serbyn, M. A. Skvortsov, and A. A. Varlamov, arXiv:1012.4316.

[52] M. N. Serbyn, M. A. Skvortsov, A. A. Varlamov, and V. Galitski, Phys. Rev. Lett. **106**, 139702 (2011).

[53] A. Sergeev, M. Reizer, and V. Mitin, arXiv:1101.4186.

[54] K. Michaeli and A. M. Finkel'stein, Phys. Rev. B **80**, 214516 (2009).

[55] O. Narikiyo, arXiv:1108.1011; arXiv:1108.0815.

[56] P. Nozières and S. Schmitt-Rink, J. Low Temp. Phys. **59**, 195 (1985).

[57] In the calculation of $\chi_{\rm Pauli}$, the free electron mass m is replaced by the effective band mass of the cuprates. This effect leads to an extra factor of roughly 0.3 in $\chi_{\rm Pauli}$.

[58] At this critical doping the pair mass becomes infinitely heavy, leading to a quartic (q^4) pair dispersion, which suppresses both T_c and T_χ down to zero.

[59] O. Cyr-Choinière, R. Daou, F. Laliberté, C. Collignon, S. Badoux, D. LeBoeuf, J. Chang, B. J. Ramshaw, D. A. Bonn, W. N. Hardy, R. Liang, J.-Q. Yan, J.-G. Cheng, J.-S. Zhou, J. B. Goodenough, S. Pyon, T. Takayama, H. Takagi, N. Doiron-Leyraud, and L. Taillefer, Phys. Rev. B **97**, 064502 (2018).

[60] H. Fukuyama, Prog. Theor. Phys. **45**, 704 (1971).

[61] R. S. Thompson, Phys. Rev. B **1**, 327 (1970).